International Journal of Solids and Structures 339 (2026) 114124

Contents lists available at ScienceDirect

International Journal of Solids and Structures

journal homepage: www.elsevier.com/locate/ijsolstr

Numerical calibration of stress-state-dependent regularization for ductile failure in shell elements

Thomas Zink [a,b], Frank Burbulla [a], Thomas Böhlke [b,*]

[a] Porsche Research and Development Centre, Weissach, Germany
[b] Karlsruhe Institute of Technology (KIT), Institute of Engineering Mechanics, Karlsruhe, Germany

ARTICLE INFO

Keywords:
Mesh dependence
Localization
Regularization
Ductile failure
GISSMO

ABSTRACT

Accurate crash simulations require robust regularization strategies to obtain mesh-independent predictions of ductile damage and fracture on coarse shell meshes. Although the GISSMO damage model is widely used to model stress-state-dependent failure, its regularization is typically calibrated from tensile tests only and relies on prescribed bi- or trilinear stress-state dependence. This work proposes a numerical calibration procedure that enables stress-state-dependent regularization for shell elements over the considered range of plane-stress triaxialities assuming isotropic elastic behavior and von Mises plasticity with isotropic hardening. Constant-triaxiality loading of rectangular element blocks is employed to generate well-defined stress states, while traction boundary conditions are constructed from a preliminary displacement-driven simulation to allow localization to develop. Using Swift's maximum-force criterion to identify the onset of diffuse necking, the mechanical work is decomposed into pre- and post-localization contributions. Regularization factors are obtained by matching the post-localization work of coarse meshes to a reference mesh, yielding stress-state-dependent failure curves. The method is demonstrated on an aluminum sheet material and compared against established GISSMO regularizations with bilinear and trilinear triaxiality dependence. Validation on constant-triaxiality blocks, tensile and Nakajima specimens as well as a profile crush test show that the proposed regularization provides comparable or improved mesh convergence, while retaining physically motivated behavior at the end points such as negligible regularization in shear and biaxial tension. The results further highlight fundamental limits of regularization for very coarse meshes, where geometric representation errors dominate the response.

1. Introduction

Reliable prediction of material failure is crucial for obtaining good agreement between crash simulations and experimental results. In crash simulations, material degradation and fracture are commonly represented using continuum damage models (Besson, 2010). Within this class, micromechanically motivated approaches, such as the Gurson model (Gurson, 1977) and extensions including the Gurson–Tvergaard–Needleman formulation (Tvergaard and Needleman, 1984) relate the macroscopic response to void nucleation, growth and coalescence. Phenomenological frameworks such as the Lemaitre damage model (Lemaitre, 1985; Chaboche, 1988) describe damage evolution through constitutive relations derived from thermodynamic potentials. For isotropic damage, a scalar variable is typically introduced to account for the reduction of the effective load-bearing area, accompanied by the effective stress concept. Such a strategy also underlies the Generalized Incremental Stress State-dependent damage Model GISSMO (Andrade et al., 2016; Neukamm, 2018).

GISSMO is widely used to predict damage and fracture of metallic materials in crashworthiness simulations and increasingly in sheet-metal forming analyses. Applications span a broad range of materials, including various steel grades as well as lightweight alloys. Extensions to non-metallic materials have also been reported. Anderson et al. (2017) calibrated a GISSMO failure surface for DP780 based on butterfly tests and reported good agreement with experiments. GISSMO has been used to predict crack formation in forming processes, e.g. for roll forming of DP980 at different temperatures (Mehari and Han, 2022) and to simulate component failure for the same material (Hong et al., 2019). For high-strength martensitic steels with tensile strengths of 1500 MPa and 2000 MPa, Guo et al. (2023, 2024) calibrated the model using tensile tests and validated it on component-level experiments, including B-pillar and hat-profile tests. Dai et al. (2022) established a triaxiality-dependent GISSMO damage and fracture calibration for quenched 22MnB5 steel and demonstrated its predictive capability

---

[*] Corresponding author.
E-mail address: thomas.boehlke@kit.edu (T. Böhlke).

https://doi.org/10.1016/j.ijsolstr.2026.114124
Received 24 February 2026; Received in revised form 7 May 2026; Accepted 25 May 2026

in crushing tests of uniform- and graded-strength profiles. Samadian et al. (2020) coupled GISSMO with a micromechanical homogenization approach for the flow response to capture failure in tailored hot-stamped steels. Beyond steels, GISSMO has been successfully applied to aluminum alloys. Chen et al. (2024) applied GISSMO to model ductile damage and fracture of a 2000-series alloy under dynamic loading. For cold forming of a 5000-series alloy, Mohamed et al. (2021) benchmarked several damage models for forming and found GISSMO to perform well overall, while noting deviations in the prediction of minor strain. Lee et al. (2018) predicted damage and fracture in roll forming of a 7000-series alloy. Yao et al. (2025) calibrated GISSMO for a 6000-series alloy using different specimen geometries to construct triaxiality-dependent instability and failure loci. In crashworthiness analysis of hybrid CFRP-Al structures, GISSMO was employed for the aluminum layers (Mou et al., 2025). Finally, GISSMO has been explored for materials beyond conventional steels and aluminum, including magnesium alloys (Choi et al., 2024) and thermoplastics (Werling et al., 2020, 2021). Moreover, applications to specific joining elements such as bolts have been reported (Gu et al., 2022; Schauwecker et al., 2022).

A fundamental challenge in crash analysis is the pronounced separation of scales. Ductile failure mechanisms evolve on microstructural length scales that cannot be resolved in full-vehicle models where the dimensions of the represented structure are orders of magnitude larger. Consequently, fracture can only be captured in an effective, homogenized sense using continuum damage formulations and relatively coarse discretizations, which makes the numerical response sensitive to the discretization length and necessitates appropriate regularization.

Parameter identification for GISSMO in sheet metals is commonly based on testing different specimen geometries, including flat dog-bone samples, shear specimens and notched tensile specimens (Effelsberg et al., 2012; Xiao and Hu, 2019). Using such a set of tests enables calibration of the failure response under different stress states. In practice, identification is typically carried out on refined shell meshes with element edge lengths of 0.5 mm, while full-vehicle crash models are usually discretized with shell elements of 3 to 5 mm to meet runtime constraints. Since localization renders failure predictions mesh-dependent (Forest and Lorentz, 2004), parameters identified at the specimen level cannot be transferred to coarse-mesh crash models without additional regularization.

An experimental option to reduce this mismatch is to calibrate the model directly on coarse meshes using enlarged specimens, such that the specimen geometry can be represented with comparatively large elements (Jurendic and Anderson, 2019). However, this largely increases the amount of material required in testing. Numerically, regularization strategies introduce a characteristic length scale into the constitutive description. Regularization in GISSMO is implemented via element-size dependent material parameters. Although GISSMO accounts for stress-state-dependent failure strain, regularization is commonly calibrated using tensile tests only, evaluated with different finite element discretizations (Effelsberg et al., 2012; Chen et al., 2018). The stress-state dependence itself is prescribed by bi- or trilinear functions in triaxiality space and recent work has proposed refinements of these functional forms (Andrade et al., 2023).

Comparable regularization concepts based on tensile tests are reported in several studies. Barba's law (Yamada et al., 2005) predicts that the local failure strain depends on the gauge length. Building on this idea, Wiegard and Ehlers (2020) calibrated mesh-specific yield curves using different extensiometer lengths in a tensile test. Kõrgesaar et al. (2014) numerically investigated the element-size dependence of the fracture strain under uniaxial tension, plane-strain tension and equibiaxial tension. They showed that the magnitude of mesh dependence is affected by the stress state due to differences in the associated localization patterns. Walters (2014) proposed a framework in which the strain from localization to failure is scaled independently for each stress state as a function of element size. Wei et al. (2021) applied an adapted version of this scheme for a modified Mohr–Coulomb model. Pack and Mohr (2017) proposed a Domain of Shell-to-Solid Equivalence (DSSE), within which shell elements reproduce the behavior of solid elements. The DSSE is limited by localized necking, identified through a Marciniak–Kuczynski analysis. They combined the DSSE with a Hosford–Coulomb failure criterion for the shell elements. An application can be found in Pack et al. (2018). Costas et al. (2019) used a Cockcroft–Latham failure criterion and distinguished between membrane and bending loading. They applied regularization only in membrane loading to the failure energy for larger elements and achieved good agreement with experiments. While these approaches represent important steps toward stress-state-dependent regularization, a comprehensive calibration strategy applicable to shell elements across the full stress-state space and suitable for coarse-mesh crash discretizations remains challenging.

This paper proposes a procedure to calibrate stress-state-dependent regularization based on membrane loading of rectangular finite-element blocks under prescribed triaxialities that remain approximately constant up to the onset of necking and introduces a consistent methodology to assess regularization performance. Parts of this work have previously been reported in Zink et al. (2025). The present paper extends the approach and provides additional validation. Section 2 summarizes the GISSMO damage model, including its constitutive relations and key material parameters. Section 3 reviews the mechanisms of localization and their impact on mesh dependence. The proposed calibration scheme is detailed in Section 4. Finally, Section 5 demonstrates the approach on both coupon- and component-level examples.

2. The GISSMO damage model

For the sake of simplicity, the constitutive equations are given in a hyperelastic small-strain setting (De Souza Neto et al., 2008), whereas LS-Dyna uses a hypoelastic co-rotational formulation based on the Jaumann stress rate (ANSYS Inc., 2023). Von Mises elastoplasticity with isotropic hardening is considered. The strain $\boldsymbol{\varepsilon}$ is split additively into an elastic contribution $\boldsymbol{\varepsilon}_{\mathrm{e}}$ and a plastic contribution $\boldsymbol{\varepsilon}_{\mathrm{p}}$. This yields

$$\boldsymbol{\varepsilon} = \boldsymbol{\varepsilon}_{\mathrm{e}} + \boldsymbol{\varepsilon}_{\mathrm{p}} \tag{1}$$

Elasticity is governed by Hooke's law. In the isotropic case, the stiffness tensor $\mathbb{C}$ is fully characterized by two independent material parameters, for instance Young's modulus E and Poisson's ratio ν. The Cauchy stress $\boldsymbol{\sigma}$ is calculated from the elastic strain as

$$\boldsymbol{\sigma} = \mathbb{C}[\boldsymbol{\varepsilon}_{\mathrm{e}}] = \frac{E}{1+\nu}\left(\boldsymbol{\varepsilon}_{\mathrm{e}} + \frac{\nu}{1-2\nu}\operatorname{tr}(\boldsymbol{\varepsilon}_{\mathrm{e}})\boldsymbol{I}\right) \tag{2}$$

The yield function for von Mises plasticity can be stated as

$$\boldsymbol{\Phi}(\boldsymbol{\sigma}, \varepsilon_{\mathrm{pv}}) = \sigma_{\mathrm{vM}}(\boldsymbol{\sigma}) - \sigma_{\mathrm{F}}(\varepsilon_{\mathrm{pv}}) = 0 \tag{3}$$

The von Mises stress σ_{vM} is defined through the norm of the deviatoric stress $\boldsymbol{\sigma}'$

$$\sigma_{\mathrm{vM}}(\boldsymbol{\sigma}) = \sqrt{\frac{3}{2}}\|\boldsymbol{\sigma}'\| \tag{4}$$

$\sigma_{\mathrm{F}}(\varepsilon_{\mathrm{pv}})$ describes the hardening characteristic of the material. The yield function is complemented by an associated flow rule

$$\dot{\boldsymbol{\varepsilon}}_{\mathrm{p}} = \dot{\gamma}\frac{\partial \boldsymbol{\Phi}}{\partial \boldsymbol{\sigma}} = \dot{\gamma}\frac{\partial \sigma_{\mathrm{vM}}}{\partial \boldsymbol{\sigma}} \tag{5}$$

$\dot{\gamma}$ denotes the plastic multiplier. The loading and unloading conditions can be stated as

$$\boldsymbol{\Phi} \le 0,\ \dot{\gamma} \ge 0,\ \boldsymbol{\Phi}\dot{\gamma} = 0 \tag{6}$$

Finally, the equivalent plastic strain is defined as

$$\dot{\varepsilon}_{\mathrm{pv}} = \sqrt{\frac{2}{3}}\|\dot{\boldsymbol{\varepsilon}}_{\mathrm{p}}\| \tag{7}$$

GISSMO builds on the elastoplastic model and extends it to include damage. Damage evolution is characterized by a scalar internal variable

D, where $D = 0$ corresponds to the intact material state and $D = 1$ marks complete damage (Andrade et al., 2016; Neukamm, 2018). Damage accumulates driven by the equivalent plastic strain $\varepsilon_{\mathrm{pv}}$ and depends on the stress state. For shell elements a plane stress state is assumed, which can be described unambiguously using the triaxiality η defined as

$$\eta = -\frac{p}{\sigma_{\mathrm{vM}}} \tag{8}$$

Here, p denotes the hydrostatic pressure and σ_{vM} is the von Mises stress. The damage evolution is given by

$$\dot{D} = \frac{n D^{1-\frac{1}{n}}}{\varepsilon_{\mathrm{f}}(\eta)} \dot{\varepsilon}_{\mathrm{pv}} \tag{9}$$

n is the damage exponent and $\varepsilon_{\mathrm{f}}(\eta)$ the material failure curve. In addition, an instability variable F is accumulated analogously as

$$\dot{F} = \frac{n F^{1-\frac{1}{n}}}{\varepsilon_{\mathrm{c}}(\eta)} \dot{\varepsilon}_{\mathrm{pv}} \tag{10}$$

where $\varepsilon_{\mathrm{c}}(\eta)$ is the material instability curve. The variable F governs the reduction of the Cauchy stress $\boldsymbol{\sigma}$. According to the effective stress concept (Lemaitre, 1985), the damaged material loaded with the Cauchy stress $\boldsymbol{\sigma}$ behaves like an undamaged material loaded with the effective stress $\tilde{\boldsymbol{\sigma}}$. Once $F = 1$ is reached, the current damage value is stored as D_{crit}. Introducing the scalar fading exponent m, the Cauchy stress $\boldsymbol{\sigma}$ is obtained from $\tilde{\boldsymbol{\sigma}}$ as

$$\boldsymbol{\sigma} = \tilde{\boldsymbol{\sigma}} \left[1 - \left(\frac{D - D_{\mathrm{crit}}}{1 - D_{\mathrm{crit}}} \right)^{m} \right] \quad \text{if} \quad F = 1 \tag{11}$$

The failure curve $\varepsilon_{\mathrm{f}}(\eta)$ and the instability curve $\varepsilon_{\mathrm{c}}(\eta)$ constitute the primary material characteristics in GISSMO. For the failure curve, established fracture concepts such as the Cockcroft–Latham criterion (Cockcroft and Latham, 1968) or the Johnson–Cook criterion (Johnson and Cook, 1985) can be represented in the triaxiality-failure strain space. More generally, GISSMO does not impose a fixed functional form, such that arbitrary failure and instability curves can be prescribed. The instability curve may be interpreted to mark the onset of localization and subsequent mesh dependence (DuBois et al., 2022). Since the fading exponent m can be specified individually for different element sizes, the post-instability stress degradation can be adapted per mesh as a practical regularization mechanism. Regularization in GISSMO mainly relies on scaling the failure curve as a function of element size. The scaling factor depends on the stress state, yielding element-size dependent failure curves of the form

$$\varepsilon_{\mathrm{f}}(\eta, \ell) = \varepsilon_{\mathrm{f}}(\eta, \ell_0) \alpha_{\mathrm{reg}}(\eta, \ell) \tag{12}$$

Here, ℓ denotes the element size and ℓ_0 the reference element size at which the failure curve has been calibrated. GISSMO provides several options for the triaxiality dependence of α_{reg}. As state of the art, a bi- or trilinear dependence is assumed (Andrade et al., 2023). In the bilinear setting, full regularization is applied in uniaxial tension $\eta = 1/3$, while the switches `BIAXF` and `SHRF` control the regularization level in biaxial tension $\eta = 2/3$ and shear $\eta = 0$. Linear interpolation is performed between these points. In the trilinear setting, the switches `RGTR1` and `RGTR2` define a triaxiality interval in which full regularization is applied. In shear and biaxial stress states, no regularization is performed. Regularization is neglected for negative triaxialities, since sheet metals are generally not expected to fail under compressive loading.

3. Localization and mesh dependence

In finite element analysis, a major source of mesh dependence is localization. Localization is commonly classified into diffuse and localized necking (Bouktir et al., 2018), which can be linked to geometrical and pathological forms of mesh dependence, respectively. In tensile testing of sheet metals, diffuse necking is typically associated with the loss of uniform deformation at the maximum uniform strain, whereas localized necking develops at later stages when deformation concentrates into a narrow band with a characteristic width on the order of the sheet thickness. A variety of criteria has been proposed to detect the onset of diffuse and localized necking, see Bouktir et al. (2018) and Abed-Meraim et al. (2014) for an overview. In this work, emphasis is put on diffuse necking and Swift's maximum force criterion (Swift, 1952).

3.1. *Diffuse necking: Swift's maximum force criterion*

In the following, Swift's criterion is considered in a restricted form. Proportional biaxial membrane tension without in-plane shear is considered, such that the loading directions coincide with the principal stress directions. The principal Cauchy stresses in-plane are denoted as σ_1 and σ_2, the out-of-plane stress as $\sigma_3 = 0$ and the principal logarithmic strains as ε_1, ε_2, ε_3.

The in-plane force resultants can be computed as $F_1 = \sigma_1 A_1$ and $F_2 = \sigma_2 A_2$ with the current areas $A_1 = \ell_2 t$ and $A_2 = \ell_1 t$, where ℓ_1 and ℓ_2 denote the current in-plane lengths and t the current sheet thickness. The forces are assumed to obtain their maximum values and remain unaffected by an incipient localization, i.e., $\mathrm{d}F_1 = 0$ and $\mathrm{d}F_2 = 0$. Differentiation of $F_1 = \sigma_1 \ell_2 t$ gives

$$0 = \frac{\mathrm{d}F_1}{F_1} = \frac{\mathrm{d}\sigma_1}{\sigma_1} + \frac{\mathrm{d}\ell_2}{\ell_2} + \frac{\mathrm{d}t}{t} = \frac{\mathrm{d}\sigma_1}{\sigma_1} + \mathrm{d}\varepsilon_2 + \mathrm{d}\varepsilon_3 \tag{13}$$

An analogous relation holds for F_2. Assuming small elastic strain increments at the onset of necking, $\mathrm{d}\varepsilon_1 \simeq \mathrm{d}\varepsilon_{\mathrm{p}1}$, $\mathrm{d}\varepsilon_2 \simeq \mathrm{d}\varepsilon_{\mathrm{p}2}$ and $\mathrm{d}\varepsilon_3 \simeq \mathrm{d}\varepsilon_{\mathrm{p}3}$ hold. Using plastic incompressibility $\mathrm{d}\varepsilon_{\mathrm{p}1} + \mathrm{d}\varepsilon_{\mathrm{p}2} + \mathrm{d}\varepsilon_{\mathrm{p}3} = 0$, one obtains $\mathrm{d}\varepsilon_1 = -(\mathrm{d}\varepsilon_2 + \mathrm{d}\varepsilon_3)$ and hence for admissible stress and strain increments

$$\mathrm{d}\sigma_1 = \sigma_1 \,\mathrm{d}\varepsilon_1 \quad \text{and} \quad \mathrm{d}\sigma_2 = \sigma_2 \,\mathrm{d}\varepsilon_2 \tag{14}$$

This can also be stated in rate form as $\dot{\sigma}_1 = \sigma_1 \dot{\varepsilon}_1$ and $\dot{\sigma}_2 = \sigma_2 \dot{\varepsilon}_2$. Again, if elastic strain increments are neglected, the total strain rate and the plastic strain rate can be used interchangeably. Eq. (14) is a consequence of constant force resultants and plastic volume conservation. This argument is specific to the case where the principal stress directions correspond to the direction of the boundary conditions, as given in Section 4.1.

To express Swift's criterion in terms of von Mises stress and equivalent strain, the plastic power is considered through the work-equivalent relation

$$\sigma_{\mathrm{vM}} \dot{\varepsilon}_{\mathrm{pv}} = \boldsymbol{\sigma} \cdot \dot{\boldsymbol{\varepsilon}}_{\mathrm{p}} \tag{15}$$

For plane stress in the principal directions, this reduces to

$$\boldsymbol{\sigma} \cdot \dot{\boldsymbol{\varepsilon}}_{\mathrm{p}} = \sigma_1 \dot{\varepsilon}_{\mathrm{p}1} + \sigma_2 \dot{\varepsilon}_{\mathrm{p}2} \tag{16}$$

Using the associated flow direction in von Mises plasticity from Eq. (5) for the plastic strain rates in 1- and 2-direction and expressing the von Mises stress as a scalar function of the principal stresses, $\sigma_{\mathrm{vM}} = \sigma_{\mathrm{vM}}(\sigma_1, \sigma_2)$,

$$\dot{\varepsilon}_{\mathrm{p}1} = \dot{\gamma} \frac{\partial \sigma_{\mathrm{vM}}}{\partial \sigma_1} \quad \text{and} \quad \dot{\varepsilon}_{\mathrm{p}2} = \dot{\gamma} \frac{\partial \sigma_{\mathrm{vM}}}{\partial \sigma_2} \tag{17}$$

follows. The plastic work can be expressed as

$$\begin{aligned} \sigma_{\mathrm{vM}} \dot{\varepsilon}_{\mathrm{pv}} &= \sigma_1 \dot{\varepsilon}_{\mathrm{p}1} + \sigma_2 \dot{\varepsilon}_{\mathrm{p}2} \\ &= \dot{\gamma} \left[\sigma_1 \left(\frac{\partial \sigma_{\mathrm{vM}}}{\partial \sigma_1} \right) + \sigma_2 \left(\frac{\partial \sigma_{\mathrm{vM}}}{\partial \sigma_2} \right) \right] \end{aligned} \tag{18}$$

For the rate of von Mises stress,

$$\begin{aligned} \dot{\sigma}_{\mathrm{vM}} &= \frac{\partial \sigma_{\mathrm{vM}}}{\partial \sigma_1} \dot{\sigma}_1 + \frac{\partial \sigma_{\mathrm{vM}}}{\partial \sigma_2} \dot{\sigma}_2 \\ &= \dot{\gamma} \left[\sigma_1 \left(\frac{\partial \sigma_{\mathrm{vM}}}{\partial \sigma_1} \right)^2 + \sigma_2 \left(\frac{\partial \sigma_{\mathrm{vM}}}{\partial \sigma_2} \right)^2 \right] \end{aligned} \tag{19}$$

results. Eliminating $\dot{\gamma}$ yields Swift's criterion in terms of von Mises stress and equivalent strain

$$\frac{\mathrm{d}\sigma_{\mathrm{vM}}}{\mathrm{d}\varepsilon_{\mathrm{pv}}} = \sigma_{\mathrm{vM}} \frac{\sigma_1 \left(\frac{\partial \sigma_{\mathrm{vM}}}{\partial \sigma_1}\right)^2 + \sigma_2 \left(\frac{\partial \sigma_{\mathrm{vM}}}{\partial \sigma_2}\right)^2}{\sigma_1 \left(\frac{\partial \sigma_{\mathrm{vM}}}{\partial \sigma_1}\right) + \sigma_2 \left(\frac{\partial \sigma_{\mathrm{vM}}}{\partial \sigma_2}\right)} \tag{20}$$

Introducing the principal stress ratio $a = \sigma_2/\sigma_1$, the von Mises principal stress can be expressed as

$$\sigma_{\mathrm{vM}} = \sqrt{\sigma_1^2 + \sigma_2^2 - \sigma_1\sigma_2} = \sigma_1\sqrt{1 - a + a^2} \tag{21}$$

The derivatives in Eq. (20) follow as

$$\frac{\partial \sigma_{\mathrm{vM}}}{\partial \sigma_1} = \frac{\sigma_1(2-a)}{2\sigma_{\mathrm{vM}}} = \frac{2-a}{2\sqrt{1-a+a^2}} \tag{22}$$

$$\frac{\partial \sigma_{\mathrm{vM}}}{\partial \sigma_2} = \frac{\sigma_1(2a-1)}{2\sigma_{\mathrm{vM}}} = \frac{2a-1}{2\sqrt{1-a+a^2}} \tag{23}$$

Inserting above expressions into Eq. (20) and simplifying yields

$$\frac{\mathrm{d}\sigma_{\mathrm{vM}}}{\mathrm{d}\varepsilon_{\mathrm{pv}}} = \sigma_{\mathrm{vM}} \frac{4a^3 - 3a^2 - 3a + 4}{4(1-a+a^2)^{3/2}} \tag{24}$$

For proportional loading with $\sigma_{\mathrm{vM}} = \sigma_{\mathrm{F}}$, these conditions can be evaluated numerically, if the material flow curve, i.e., $\sigma_{\mathrm{F}}(\varepsilon_{\mathrm{pv}})$, is known in tabulated form. Other criteria for diffuse necking based on bifurcation analysis exist, for instance Hill's General Bifurcation Criterion (GBC) (Hill, 1958; DuBois et al., 2022).

3.2. Geometrical mesh dependence

Geometrical mesh dependence arises when the finite element discretization is coarser than the characteristic length of the diffuse localization zone (Storheim et al., 2015). In this case, the degrees of freedom provided by the mesh are insufficient to resolve the evolving deformation pattern and the associated geometry changes, which makes this mechanism particularly relevant for crash simulations.

A possible remedy is to introduce mesh-dependent material parameters, as outlined in Section 1. While this does not eliminate mesh sensitivity entirely, it can substantially reduce its effects in practical applications.

3.3. Localized necking: Loss of ellipticity or hyperbolicity

Localized necking develops after the onset of diffuse necking, when the governing boundary value problem loses ellipticity (Forest and Lorentz, 2004) in quasi-statics and hyperbolicity in dynamics (Belytschko and Lasry, 1989). Corresponding detection criteria are commonly formulated in terms of the acoustic tensor and its loss of positive definiteness (Bouktir et al., 2018; Rabczuk, 2013). Localized necking is not specifically considered in the following.

3.4. Pathological mesh dependence

Pathological (Needleman, 1988) or spurious (Bažant and Jirásek, 2002) mesh dependence refers to deformation localizing into a single row of finite elements and is primarily associated with localized necking. In continuum damage models, this typically results in earlier predicted failure for smaller elements. To mitigate pathological mesh dependence, nonlocal approaches (Davaze et al., 2023; Andrade et al., 2009) introduce gradient-based or integral measures into the damage model to transfer information across neighboring elements. Viscous regularization methods (Niazi et al., 2013; Geers et al., 1994) introduce a viscosity into the constitutive response, thereby limiting localization. Variational relaxation of the incremental energy has also been proposed as an alternative route to restore mesh objectivity in local softening damage models. The original ill-posed incremental energy of a local softening damage model is replaced by a relaxed envelope, allowing energetically admissible mixtures of damage states and thereby avoiding pathological mesh dependence (Schwarz et al., 2021; Lauff et al., 2026). Pathological mesh dependence is mainly critical when the finite elements are smaller than the characteristic length of the localization zone, which is typically not the case in crash simulations.

3.5. Quantification of mesh dependence

To quantify mesh dependence, an error measure that enables a direct comparison between simulations with different finite element discretizations is required. Regularization performance is assessed based on the mechanical work W. On integration point level, W can be defined as

$$W = \int_{t_0}^{t_1} \boldsymbol{\sigma} \cdot \dot{\boldsymbol{\varepsilon}} \, \mathrm{d}t \tag{25}$$

W comprises both recoverable stored energy and irreversible dissipation. Without a full thermodynamic specification, the split between stored and dissipated energy cannot be uniquely identified. For coupon and component tests, the external work W corresponding to the area under the force–displacement curve can be evaluated instead

$$W = \int_{u_0}^{u_1} F_{\mathrm{ext}} \, \mathrm{d}u \tag{26}$$

A scalar error between a reference mesh and a target mesh is computed as

$$\mathrm{error}(\ell) = \frac{W(\ell) - W_{\mathrm{ref}}}{W_{\mathrm{ref}}} \tag{27}$$

W_{ref} denotes the work on the reference mesh and $W(\ell)$ the work on a mesh with element size ℓ. A positive sign indicates that more work is required for larger meshes, a negative sign the opposite. Smaller values in terms of magnitude correspond to better regularization. Additionally, the stress–strain and force–displacement curves as well as the distribution of equivalent plastic strain prior to failure can be evaluated. In this study, the reference element size is 0.5 mm, while element sizes 1, 2, 3 and 5 mm are considered as target discretizations.

4. Numerical calibration of regularization curves

4.1. Imposing constant triaxialities

To enable a complete stress-state-dependent regularization, it is desirable to load geometries with different mesh resolutions under constant triaxialities. In this work, an approach proposed by Andrade et al. (2022) is adopted. For plane stress, the stress tensor can be expressed in terms of principal stresses and decomposed into a hydrostatic part $\boldsymbol{\sigma}^\circ$ and a deviatoric part $\boldsymbol{\sigma}'$. The components of the hydrostatic part follow as

$$\boldsymbol{\sigma}^\circ \hat{=} \sigma \begin{pmatrix} \frac{a+1}{3} & 0 & 0 \\ 0 & \frac{a+1}{3} & 0 \\ 0 & 0 & \frac{a+1}{3} \end{pmatrix} \tag{28}$$

The components of the deviatoric part read

$$\boldsymbol{\sigma}' \hat{=} \sigma \begin{pmatrix} \frac{2-a}{3} & 0 & 0 \\ 0 & \frac{-1+2a}{3} & 0 \\ 0 & 0 & -\frac{1+a}{3} \end{pmatrix} \tag{29}$$

The notation $\hat{=}$ indicates that the principal coordinate system is not further specified. Calculating the hydrostatic pressure p and the von Mises Stress σ_{vM} and inserting into Eq. (8) gives the triaxiality η as a function of the stress ratio a

$$\eta = \frac{a+1}{3\sqrt{a^2 - a + 1}} \operatorname{sgn}(\sigma_1) \tag{30}$$

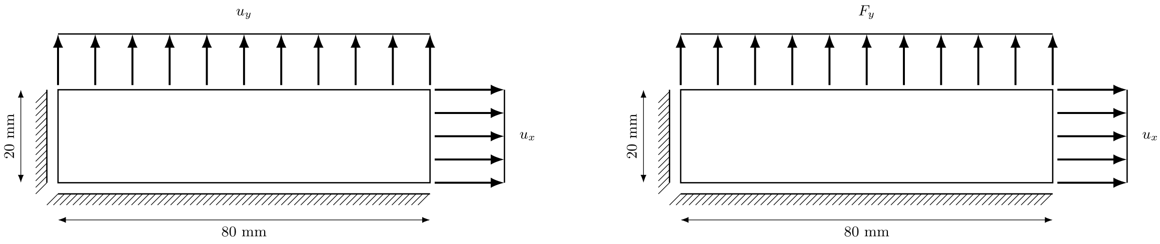

(a) Prescribed displacements in x- and y-direction

(b) Prescribed displacements in x- and tractions in y-direction

Fig. 1. Rectangular block geometry with displacement and traction boundary conditions. The traction forces are computed from the displacement-driven simulation.

In the following, $\eta \in [0, 2/3]$ is considered corresponding to $\sigma_1 > 0$ and $a \in [-1, 1]$. In this restricted range, the function $\eta(a)$ can be inverted. The inverse $a(\eta)$ reads

$$a = \frac{9\eta^2 - 3\sqrt{3}\eta\sqrt{4 - 9\eta^2} + 2}{2(9\eta^2 - 1)} \tag{31}$$

If a von Mises plastic model is assumed and the loading is proportional, i.e., the stress state does not change during deformation, the plastic strain tensor and the stress tensor are proportional with

$$\boldsymbol{\varepsilon}_{\mathrm{p}} \hat{=} \sqrt{\frac{3}{2}} \frac{\|\boldsymbol{\varepsilon}_{\mathrm{p}}\| \operatorname{sgn}(\sigma_1)}{\sqrt{a^2 - a + 1}} \begin{pmatrix} \frac{2-a}{3} & 0 & 0 \\ 0 & \frac{-1+2a}{3} & 0 \\ 0 & 0 & -\frac{1+a}{3} \end{pmatrix} \tag{32}$$

Additionally, the elastic strains are assumed to be negligible, so that $\boldsymbol{\varepsilon} \simeq \boldsymbol{\varepsilon}_{\mathrm{p}}$ holds. Then, the strain ratio b can be expressed through the stress ratio a

$$b = \frac{\varepsilon_2}{\varepsilon_1} = \frac{1 - 2a}{a - 2} \tag{33}$$

The strain ratio can thus be represented as a function of triaxiality

$$b = \frac{-3\eta^2 - \sqrt{3}\eta\sqrt{4 - 9\eta^2} + 2}{2(3\eta^2 - 1)} \tag{34}$$

For a rectangular block of elements with width w and height h, one admissible set of boundary displacements to impose this strain ratio is obtained as

$$u_x = (\exp(\varepsilon_1) - 1)w \tag{35}$$

$$u_y = (\exp(b\varepsilon_1) - 1)h \tag{36}$$

This form is adopted for simplicity of implementation and because it directly yields the desired homogeneous deformation in the rectangular domain.

If displacements are prescribed along the entire boundary of the element block, diffuse necking cannot initiate at the boundary and localization is artificially constrained. To reduce this effect, traction boundary conditions are imposed instead. First, a simulation with displacement boundary conditions is carried out and the nodal forces along the boundary are evaluated and stored. In a subsequent simulation, these forces are applied as time-dependent tractions, replacing the displacement constraints. Identical meshes with element sizes of 0.5, 1, 2, 3 and 5 mm with underintegrated shell elements (`ELFORM` = 2 in LS-Dyna) and 5 through-thickness integration points are used in both simulations. Up to the onset of necking, displacement- and traction-driven simulations yield identical responses. Once necking initiates under traction boundary conditions, the corresponding force–displacement curves start to deviate and the triaxiality changes from the prescribed value.

4.2. *Work-based regularization*

The boundary conditions described in Section 4.1 are applied to blocks with $w = 80$ mm and $h = 20$ mm as shown in Figs. 1(a) and 1(b). The triaxiality range $0 \leq \eta \leq 2/3$ is discretized into 67 equidistant points spanning $0 \leq \eta \leq 0.66$. In addition, the endpoint $\eta = 2/3$ is included. Each point is assigned an individual regularization parameter for every considered element length, resulting in a total of 272 parameters for the four target discretizations under investigation. Given the large number of parameters and simulations, a non-iterative calibration strategy is required. To this end, the mechanical work at failure is evaluated for each element block and an error according to Eq. (27) is computed. If Swift's criterion is assumed to hold and is adopted as the instability strain $\varepsilon_{\mathrm{c}}(\eta)$ in GISSMO, the mechanical work W_{total} can be decomposed into a pre-localization and a post-localization contribution

$$W_{\mathrm{total}} = W_{\mathrm{pre}} + W_{\mathrm{post}} \tag{37}$$

with

$$W_{\mathrm{pre}} = \int_0^{\min(\varepsilon_{\mathrm{c}}(\eta), \varepsilon_{\mathrm{f}}(\eta, \ell))} \sigma_{\mathrm{F}}(\varepsilon_{\mathrm{pv}})\, \mathrm{d}\varepsilon_{\mathrm{pv}} \tag{38}$$

making use of $\sigma_{\mathrm{vM}} = \sigma_{\mathrm{F}}$ for proportional loading. The instability curve $\varepsilon_{\mathrm{c}}(\eta)$ is obtained by evaluating Eq. (24) for triaxialities from 0 to 2/3. As mesh dependence starts at the onset of localization, the pre-localization contribution W_{pre} is expected to be mesh-independent, whereas the post-localization contribution W_{post} increases with element size for identical failure strains due to geometrical mesh dependence. Modifying the failure strain also affects the deformation history up to failure, because the stress reduction induced by damage alters the displacement field and the strain and stress evolution. As a result, the dependence of the post-localization work on the failure strain is generally nonlinear and governed by the material parameters. A linear relationship is considered a reasonable approximation, since the flow curve of metallic materials typically exhibits saturation at large strains, so that W_{post} becomes approximately linear with respect to the failure strain. Based on this assumption, a regularization factor is defined as

$$\tilde{\alpha}_{\mathrm{reg}}(\eta, \ell) = \frac{W_{\mathrm{post}}(\eta, \ell_0)}{W_{\mathrm{post}}(\eta, \ell)} \tag{39}$$

and applied to the failure curve via

$$\varepsilon_{\mathrm{f}}(\eta, \ell) = \varepsilon_{\mathrm{c}}(\eta) + \tilde{\alpha}_{\mathrm{reg}}(\eta, \ell)\left(\varepsilon_{\mathrm{f}}(\eta, \ell_0) - \varepsilon_{\mathrm{c}}(\eta)\right) \tag{40}$$

for all triaxialities with $\varepsilon_{\mathrm{c}}(\eta) < \varepsilon_{\mathrm{f}}(\eta, \ell_0)$. If $\varepsilon_{\mathrm{c}}(\eta) > \varepsilon_{\mathrm{f}}(\eta, \ell_0)$, W_{post} vanishes, $\tilde{\alpha}_{\mathrm{reg}}(\eta, \ell) = 1$ and effectively no regularization is applied. If for a given mesh size the post-localization work exceeds that of the reference mesh, $\tilde{\alpha}_{\mathrm{reg}}(\eta, \ell) < 1$ and regularization becomes active. Since the computed regularization factors would lead to non-smooth failure curves with respect to triaxiality due to numerical oscillations, a Gaussian filter with a standard deviation of $\sigma_{\mathrm{Gauss}} = 0.02$ in triaxiality space is applied.

5. Application and validation

5.1. *Material parameters*

To facilitate an interpretation of the proposed regularization strategy, a generic material card is employed. The elastic constants are set

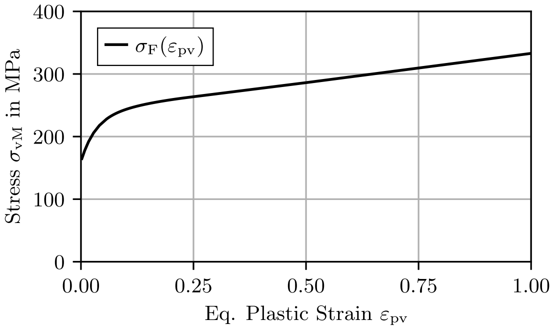

Fig. 2. Material flow curve used in the simulations.

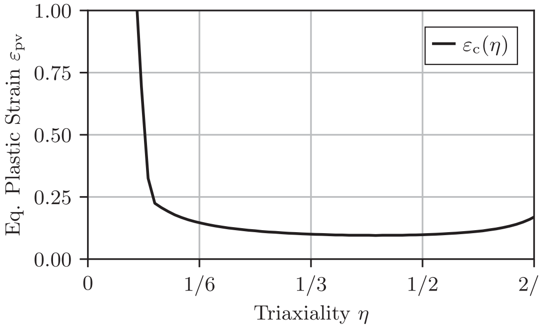

Fig. 3. Instability curve used in the simulations based on Swift's maximum force criterion for in-plane tensile loading.

to $E = 70$ GPa and $\nu = 0.3$. The material flow curve shown in Fig. 2 corresponds to a 6000 series aluminum alloy with a yield strength of 165 MPa and an ultimate tensile strength of 220 MPa. The instability curve $\varepsilon_\mathrm{c}(\eta)$ in Fig. 3 is calibrated using Swift's criterion as described in Section 3. For the fading exponent, a value of $m = 2$ is used inducing softening once the instability variable reaches $F = 1$. As softening influences mesh dependence and interacts with regularization, the results for the same material card without softening are provided in Appendix. The parameter `NUMFIP`, that controls element erosion based on the number of failed integration points, is set to −80. This means that integration points on 80 % of the planes of a shell element have to fail to trigger element erosion. The reference failure curve $\varepsilon_\mathrm{f}(\eta)$ for an element size of 0.5 mm is intentionally simplified to a constant failure strain of 1, so that the resulting regularization factors can be directly interpreted as failure strains.

5.2. Verifying constant triaxialities

To verify that the prescribed displacements and tractions in the follow-up simulation induce the intended triaxiality, the triaxiality is evaluated from the stress response. The resulting strain paths, i.e., triaxialities as a function of plastic strain, are shown in Fig. 4 for the element exhibiting the earliest failure in a 0.5 mm mesh. A similar representation was used by Andrade et al. (2022). It can be seen that the triaxiality remains constant until necking occurs and agrees with the prescribed triaxiality value. Once necking sets in, the triaxiality changes due to localization. The deviation from the prescribed triaxiality value can be interpreted as a local indicator of necking and is in good agreement with Swift's criterion. After the onset of necking, different prescribed triaxialities lead to different localization characteristics, and some of the strain paths cross. Nevertheless, the strain paths for different prescribed triaxialities are clearly distinguishable.

The decomposition of mechanical work along these strain paths is illustrated for the 0.5 mm mesh in Fig. 5. Owing to the computational procedure based on Swift's criterion, the pre-localization work W_pre closely reflects the shape of the instability curve. For the present material, W_pre exceeds the post-localization contribution W_post over the entire triaxiality range. For small triaxialities close to 0, W_pre calculated from Eq. (38) exceeds W_total, indicating that failure occurs without prior localization. The post-localization work decreases from its first non-zero value to a minimum near plane-strain loading and increases again as the triaxiality approaches 2/3.

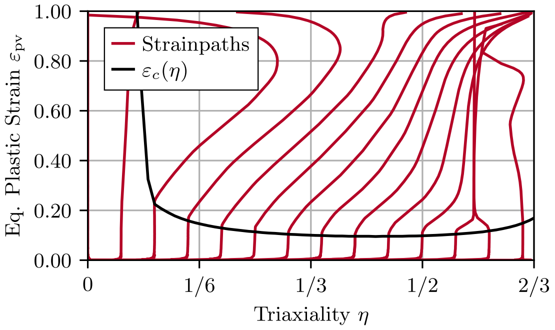

Fig. 4. Evolution of stress state as a function of plastic strain for different prescribed triaxialities. The triaxiality is constant until the onset of localization. Different stress states exhibit different localization patterns.

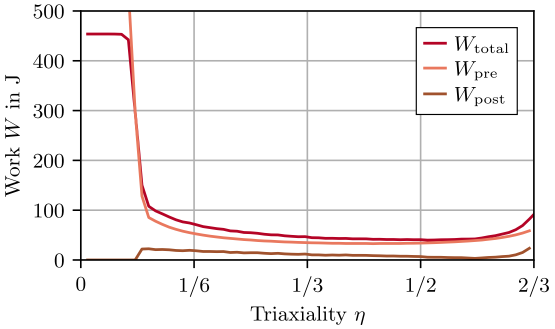

Fig. 5. Work W with contributions pre- and post-localization. The pre-localization contribution exceeds the post-localization contribution over the entire stress-state range.

5.3. Regularization approaches

Three regularization approaches are investigated for the considered material and compared to a baseline without regularization. The first variant, hereafter referred to as Approach A, assumes a bilinear stress-state dependence. Regularization is not applied in shear and biaxial tension, whereas full regularization is enforced in uniaxial tension. The corresponding regularization factor is calibrated from tensile tests evaluated on finite element meshes with different element sizes. The second variant, Approach B, follows the same calibration procedure but assumes a trilinear stress-state dependence. Full regularization is applied for $1/3 \le \eta \le 1/\sqrt{3}$, i.e., from uniaxial tension to plastic plane-strain loading, while no regularization is imposed in shear and biaxial tension with linear interpolation between the set points. As the stress-state dependence of the regularization factor differs for Approach A and B, the factors obtained by calibrating based on the same tensile specimen also differ. As described in Section 2, approaches A and B form the state of the art in GISSMO. Approach C corresponds to the numerically calibrated regularization proposed in Section 4. Fig. 6(a) shows the constant failure curve without regularization, whereas the element-size-dependent failure curves obtained with the different regularization approaches are presented in Figs. 6(b), 6(c) and 6(d). All regularization

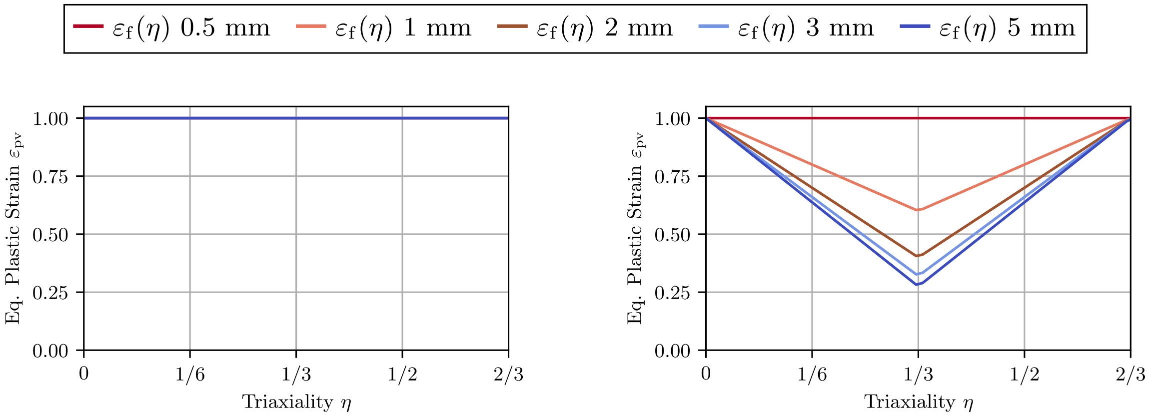

(a) No regularization

(b) Approach A

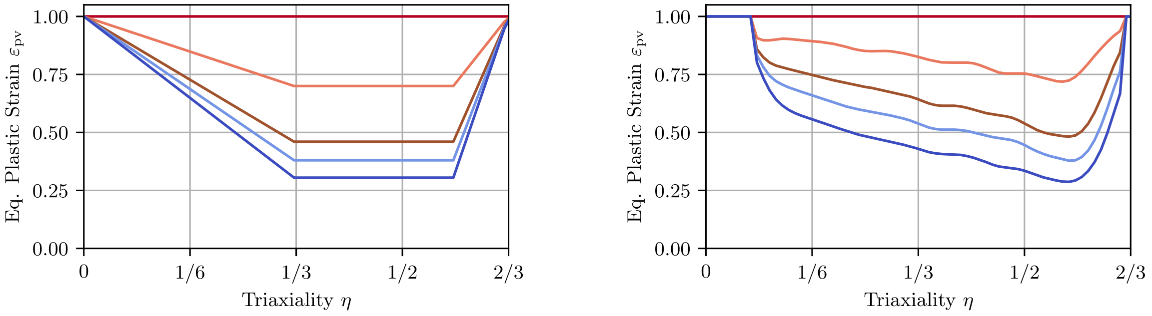

(c) Approach B

(d) Approach C

Fig. 6. Failure curves for different regularization approaches showing stress-state dependent behavior with differences in curvature and the location of minima.

approaches yield monotonically decreasing failure strains with increasing element size. The minimum failure strains are comparable across the regularization concepts, for instance approximately 0.3 for a 5 mm mesh. However, the stress-state dependence differs markedly. While approaches A and B are restricted to a piecewise linear dependence, Approach C exhibits a strongly nonlinear dependence. The failure strain remains approximately constant for stress states close to shear, then decreases towards a minimum around plane-strain tension and finally recovers to 1 in biaxial tension, where no regularization is applied.

5.4. Results on element level

The regularization performance is first assessed on the constant-triaxiality block model described in Section 4. While regularization Approach C is calibrated on this model, the simulations provide a validation case for approaches A and B.

The regularization results are presented in terms of the error for the different meshes and regularization approaches in Fig. 7. The error calculation is based on the total work to failure, i.e., $W_\mathrm{pre} + W_\mathrm{post}$. The error curves exhibit non-smooth behavior for a fixed element size, which is attributed to numerical sensitivity. Since localization is a nonlinear phenomenon, the results are sensitive to small changes in the simulation setup. For instance, reducing the velocity in the displacement-driven simulations leads to smoother curves, but also increases the computation time. A compromise between curve smoothness and computational efficiency is therefore adopted. Without regularization, errors of up to 60 % occur, cf. Fig. 7(a). Although the error magnitude depends on the stress state, the work is consistently overestimated over the entire triaxiality range. As shown in Fig. 7(b), regularization with Approach A improves the agreement, since the mechanical work obtained for different meshes moves closer to the reference level. This improvement is most pronounced for stress states in the range $0 \le \eta \le 1/3$. For stress states between uniaxial and plane-strain tension, i.e., $1/3 < \eta \le 1/\sqrt{3}$, the mechanical work remains overestimated for larger elements. Approach B reduces this overestimation and yields nearly mesh-independent results with respect to work for most stress states, as illustrated in Fig. 7(c). From plane-strain to biaxial tension, $1/\sqrt{3} < \eta \le 2/3$, deviations persist, with larger elements still exhibiting higher work values. Approaches A and B also apply regularization in stress states where localization is not expected, i.e., where $W_\mathrm{post} = 0$. The element block model indicates that this may introduce an artificial mesh dependence. The mechanical work to failure is underestimated for small triaxialities with errors of up to 15 % magnitude. This could be avoided by limiting the range of impact for both regularization approaches. However, this is not part of the current design of the approaches as they are built in and used as state of the art in GISSMO. The strongest convergence with respect to mechanical work is obtained with Approach C, which is demonstrated in Fig. 7(d) and thus supports the proposed calibration procedure. The error is below 10 % for all element sizes and stress states.

5.5. Results on specimen level

As a second verification step, the regularization approaches are evaluated on tensile and Nakajima specimens. Approaches A and B were calibrated on the tensile specimen, whereas it serves as an independent validation for the work-based regularization C. The Nakajima tests with specimen widths of 15, 45 and 85 mm induce stress states with triaxialities of approximately 0.4, $1/\sqrt{3}$ and 2/3, providing a validation case for all approaches. As an evaluation metric, the mechanical work is computed as the integral of the force–displacement curve following

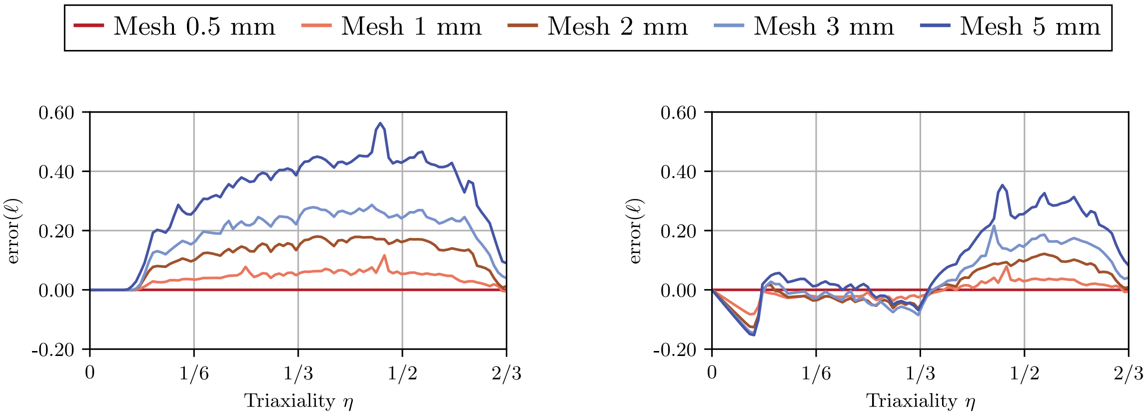

(a) No regularization

(b) Approach A

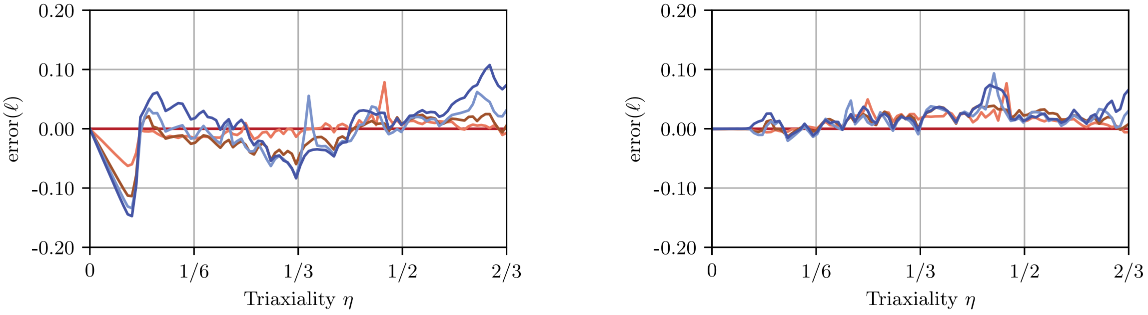

(c) Approach B

(d) Approach C

Fig. 7. Element-level errors for different regularization approaches as a function of stress triaxiality. The magnitude and variability of the error differ significantly between the approaches and depend on the element size.

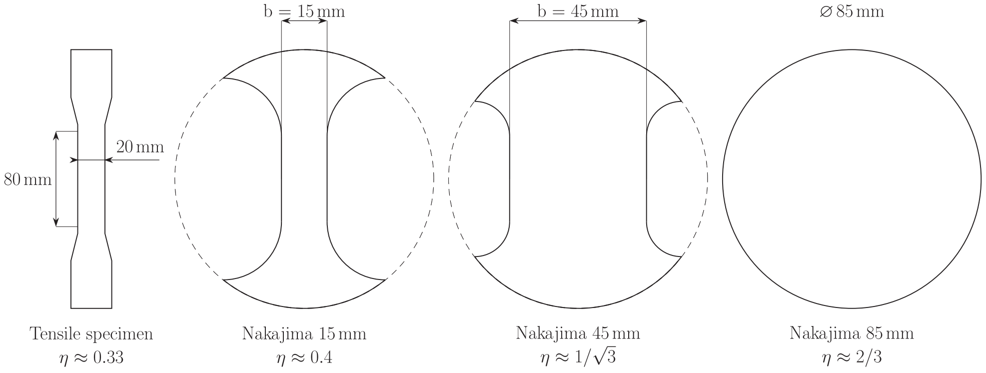

Fig. 8. Geometry of the tensile specimen and the Nakajima specimens with the corresponding stress triaxialities.

Eq. (26). A drop of 30 % with respect to the maximum stress or maximum force is used as a cutoff criterion for the integral of mechanical work in order to exclude the response after the onset of failure.

The resulting errors are shown in Fig. 9. Without regularization, all specimens exhibit a pronounced increase in work with increasing element size due to geometrical mesh dependence. This trend is strongest for the Nakajima 45 specimen, which corresponds to a stress state close to plane-strain tension at $\eta = 1/\sqrt{3}$. Consistent with this observation, the numerical calibration yields the smallest regularization factors in this regime. The weakest mesh dependence is observed for biaxial stress states, where none of the approaches applies regularization. Approach A reduces mesh dependence for all specimens. However, a systematic shift towards higher work levels for larger elements remains. Approach B further improves the results. For the Nakajima 45 specimen, the 5 mm mesh still requires roughly 50 % more work than the reference mesh. For other cases, such as the Nakajima 15 specimen, the trend reverses and work ratios below 1 are obtained. As on the element block level, Approach C and Approach B yield similar results. Approach C exhibits larger errors for the tensile test than Approach A and B. This is due to the calibration of Approach A and B on exactly this test. For the Nakajima specimens, Approach C shows advantages, especially for larger elements sizes.

When averaging the error across all specimens in Table 1, Approach B yields the lowest mean error for element sizes 1 and 2 mm, while Approach C performs best for element sizes 3 and 5 mm. Approach A and the unregularized baseline exhibit substantially larger errors.

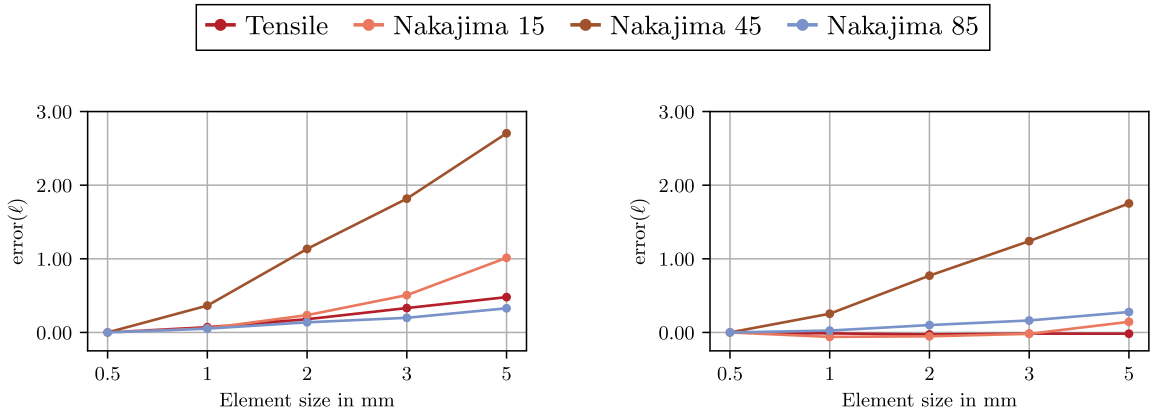

(a) No regularization

(b) Approach A

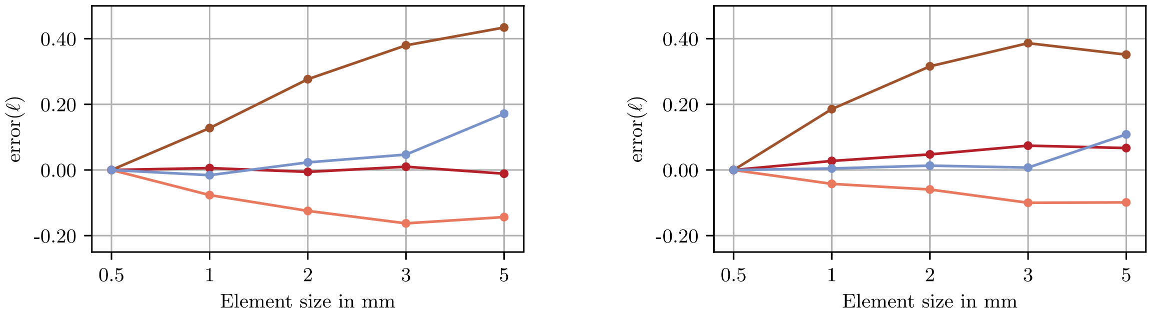

(c) Approach B

(d) Approach C

Fig. 9. Specimen-level errors for different regularization approaches. The highest error is observed for the Nakajima 45 specimen.

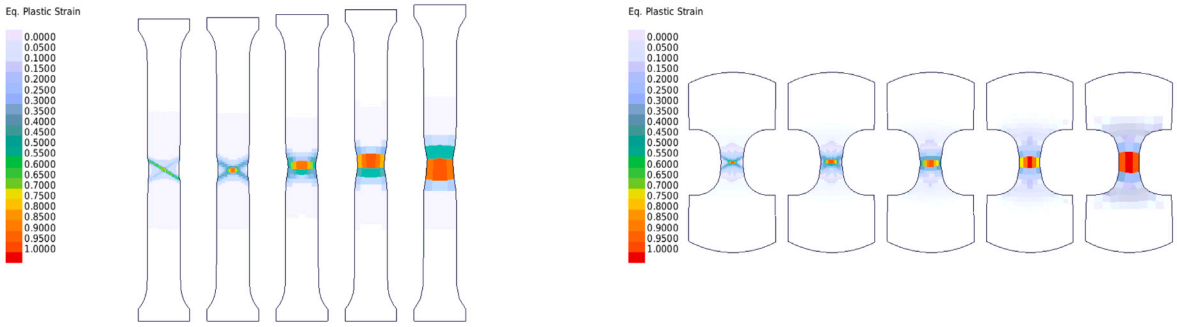

(a) Tensile specimen

(b) Nakajima 15

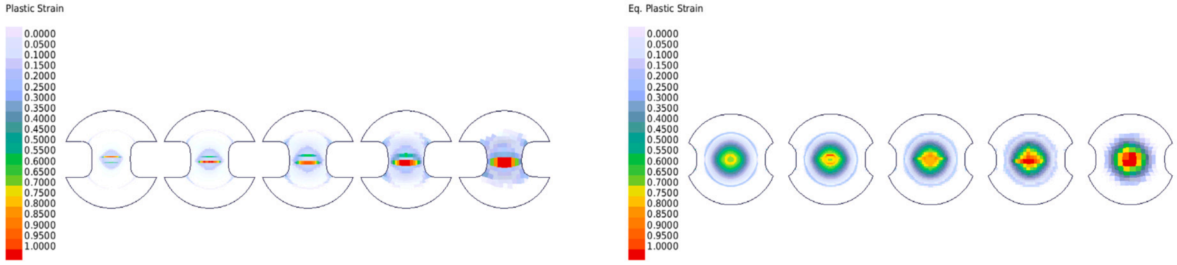

(c) Nakajima 45

(d) Nakajima 85

Fig. 10. Distribution of equivalent plastic strain prior to failure without regularization for mesh sizes 0.5, 1, 2, 3 and 5 mm. The strain patterns differ with element size.

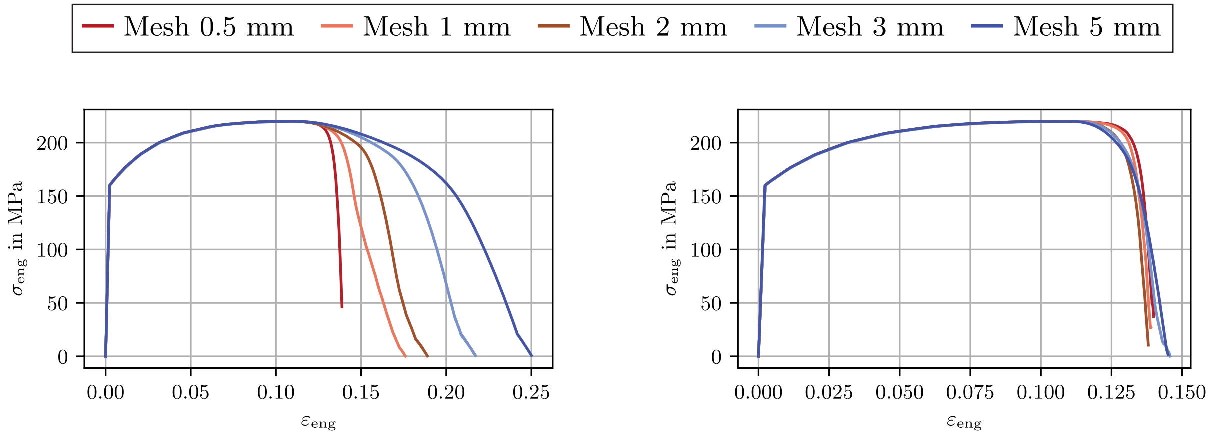

(a) No regularization

(b) Approach A

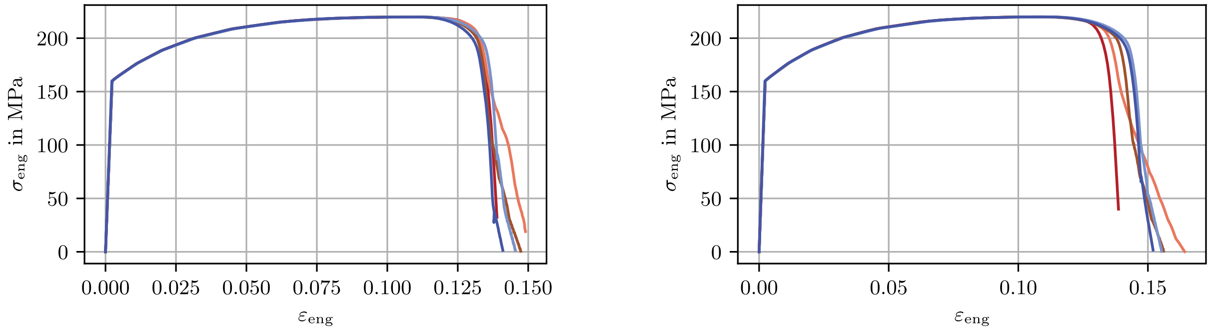

(c) Approach B

(d) Approach C

Fig. 11. Stress–strain curves for the tensile test without regularization and with regularization Approaches A–C for mesh sizes 0.5, 1, 2, 3 and 5 mm. For the regularized approaches, the failure strain is similar for all meshes, whereas without regularization the failure strain and failure displacement increase with the element size.

Table 1
Mean absolute relative work error (Eq. (27)) for different regularization approaches and shell element edge lengths. The error increases monotonically with the element size.

Approach	1 mm	2 mm	3 mm	5 mm
Baseline	0.135	0.422	0.714	1.131
A	0.088	0.238	0.359	0.548
B	0.057	0.108	0.150	0.190
C	0.065	0.109	0.114	0.156

To further evaluate the results, Fig. 10 shows the distributions of equivalent plastic strain at the last recorded state prior to failure for the baseline simulation without regularization. Since these distributions are qualitatively similar for all regularization approaches, only the baseline simulation without regularization is shown. When regularization is applied, the equivalent plastic strain at failure is reduced. Fig. 11 depicts the stress–strain curves for the tensile test obtained with the different regularization approaches. The force–displacement curves for the Nakajima tests with different specimen widths are shown in Figs. 12, 13, and 14. In the tensile test, the results for all meshes coincide up to the ultimate tensile strength, independent of regularization. Without regularization, the stress–strain curves begin to deviate once necking occurs. Because softening with $m = 2$ is active, all meshes exhibit a decrease in force. However, this decrease becomes weaker with increasing element size as necking becomes less pronounced. A 45° shear-band pattern develops for the 0.5 and 1 mm meshes, whereas for larger element sizes the plastic strain localizes in a single row of elements perpendicular to the loading direction. Without regularization, the engineering strain at failure increases with element size, corresponding to an increase in mechanical work. All regularization approaches compensate for this by reducing the failure strain for larger element sizes. Approaches A and B are calibrated on the tensile test and therefore yield very similar failure strains for all element sizes. In particular, Approach B also provides a better representation of the force decrease after the onset of necking. With Approach C, larger element sizes tend to exhibit higher failure strains. Still, there is a significant improvement over the baseline without regularization, and all meshes lie within a range of 2 % in terms of engineering strain at failure. The Nakajima 15 test also shows necking prior to failure, although it is less pronounced than in the tensile test. For the 0.5 mm mesh, this results in a visible drop in force before failure. Still, when no regularization is applied, a clear tendency toward later failure is observed with increasing element size. The distribution of equivalent plastic strain shows a 45° pattern for the 0.5 mm mesh and a localization in a single row of elements perpendicular to the loading direction for the larger meshes, similar to the tensile test. Approach A exhibits similar force and displacement levels at failure for element sizes up to 3 mm, whereas the 5 mm mesh fails later and at a higher force level. For all meshes other than the 0.5 mm mesh, no necking-induced drop in force is observed before failure. Approaches B and C show similar results across all element sizes, with a tendency toward earlier failure for 1 and 2 mm elements. Overall, all approaches provide satisfactory regularization for the Nakajima 15 test. For the Nakajima 45 test, the strongest mesh dependence is observed for all regularization approaches as well as for the unregularized baseline. The plastic strain localizes into two rows of

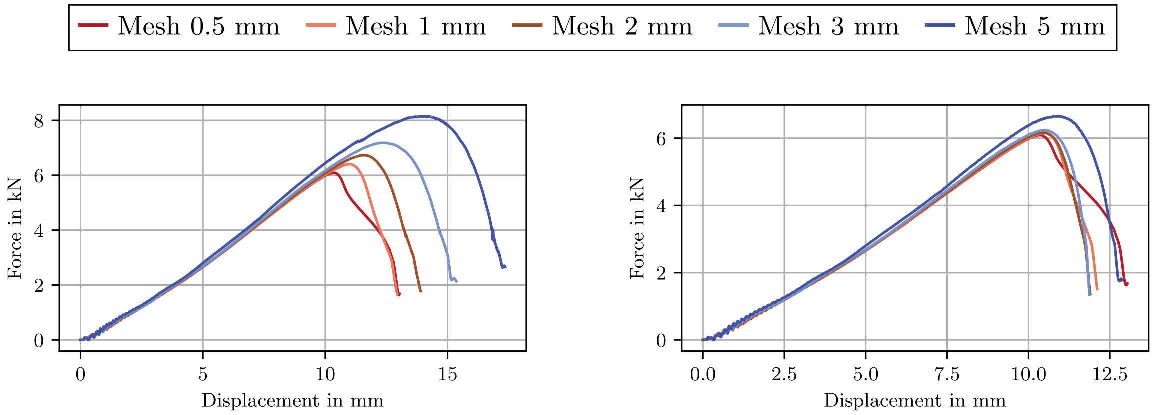

(a) No regularization

(b) Approach A

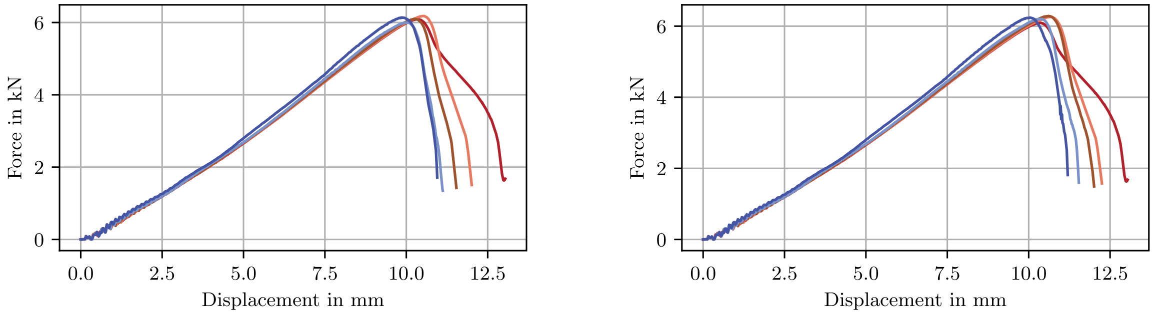

(c) Approach B

(d) Approach C

Fig. 12. Force–displacement curves for the Nakajima 15 specimen without regularization and with regularization Approaches A–C for mesh sizes 0.5, 1, 2, 3 and 5 mm. Without regularization, the maximum force and displacement at failure increase with element size.

elements for mesh sizes up to 2 mm and into a single row of elements for the 3 and 5 mm meshes. The triaxiality is close to $1/\sqrt{3}$, indicating plane-strain tension conditions. For this triaxiality, Swift's criterion predicts the onset of localization at low plastic strains. This leads to strong mesh dependence. While the 0.5 mm mesh fails at a maximum force of approximately 12 kN, the 5 mm mesh reaches up to 22 kN if no regularization is applied. Approach A reduces the maximum force, but the 5 mm mesh still reaches more than 20 kN. The reason is the bilinear stress-state dependence, for which regularization is already reduced in plane-strain tension. Approach B still applies full regularization for this triaxiality and reduces the maximum force of the 5 mm mesh to 15 kN. Approach C exhibits the strongest regularization in plane-strain tension, corresponding to a further decrease in maximum force to slightly below 15 kN. For the Nakajima 85 specimen, the plastic strain is distributed over a larger number of elements at the center of the specimen. Localization occurs only shortly before failure. The force–displacement curves show only weak mesh dependence in terms of displacement at failure. Even for the unregularized baseline, the displacements at failure lie between approximately 18 and 20 mm. Only the 5 mm mesh deviates before reaching the maximum force level. All three regularization approaches improve mesh convergence, with Approach C yielding nearly identical displacements at failure.

5.6. Results on component level

To reduce the remaining gap towards full-vehicle applications, a crush test of an extrusion profile is simulated. The profile has a length of 300 mm and is compressed by a stamp moving with constant velocity to a residual length of 100 mm. As in the previous studies, mechanical work is used as the evaluation metric for the different regularization approaches. The results, obtained by integrating force over displacement and comparing with the reference work of the 0.5 mm mesh, are shown in Fig. 15.

Overall, the differences between the approaches are small. For the coarser meshes with element sizes of 3 and 5 mm, Approach B and the numerically calibrated Approach C provide the lowest deviations in terms of mechanical work. The influence of element size is also reflected in the distribution of equivalent plastic strain shown in Fig. 16. For larger elements, localization is less pronounced, so that a larger portion of the profile participates in buckling and folding. As a result, the folding pattern changes visibly with element size. The force–displacement curves exhibit very similar overall trends for all regularization approaches. Therefore, only the force–displacement curve for the simulation without regularization is shown in Fig. 17. With coarser meshes, the initial force peak reaches higher values, whereas the subsequent force drop is more pronounced for finer meshes. After the first buckling event, the force oscillates around a mean level of approximately 50 kN. Coarser meshes tend to exhibit higher force levels. These differences in the force response arise from the element-size-dependent changes in buckling behavior. Despite element erosion occurring along the full length of the profile, the absorbed work remains more sensitive to mesh size than to the selected regularization strategy. This observation does not indicate insufficient regularization. Rather, it suggests that element erosion is a less dominant mechanism in the crush test than in, for example, the tensile test.

A further limitation of the presented regularization strategies becomes apparent at the component level. The triaxiality is not prescribed by the boundary conditions but emerges from the progressive folding of the profile. Applying nominally identical boundary conditions on different meshes can therefore lead to different stress-state histories and differences in damage accumulation. Since these mesh-induced

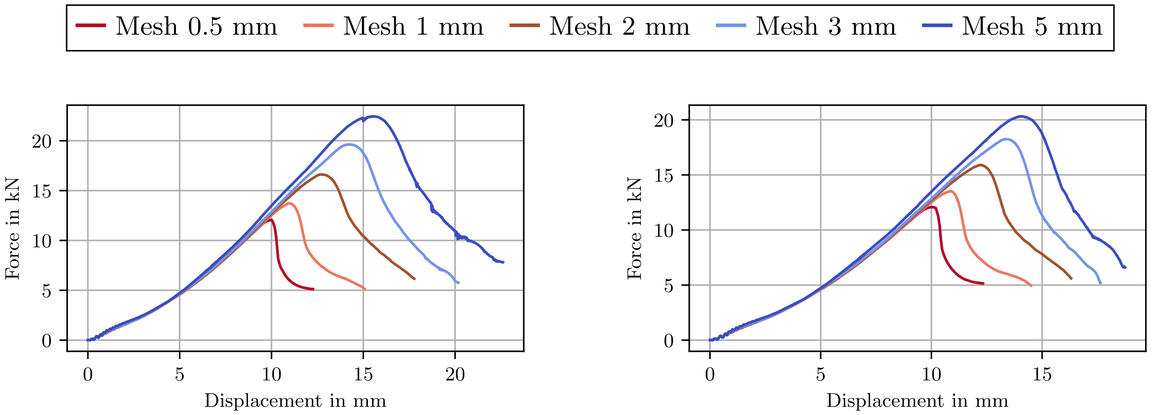

(a) No regularization

(b) Approach A

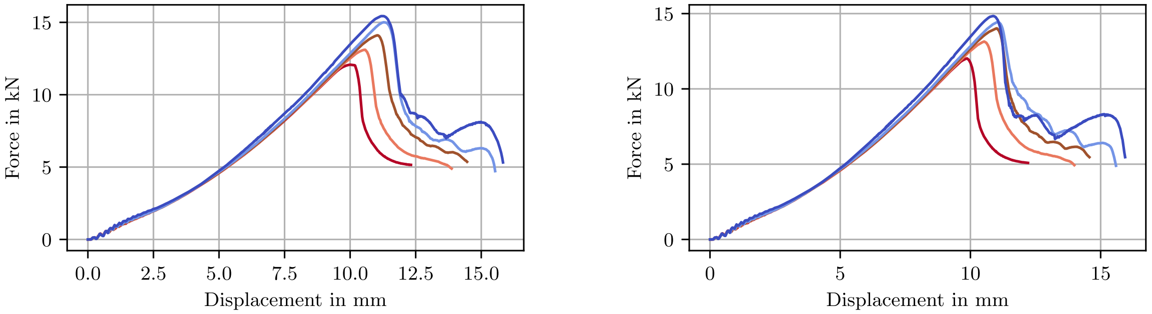

(c) Approach B

(d) Approach C

Fig. 13. Force–displacement curves for the Nakajima 45 specimen without regularization and with regularization Approaches A–C for mesh sizes 0.5, 1, 2, 3 and 5 mm. Without regularization, a strong mesh dependence is observed.

variations depend on the specific geometry and deformation mode, they cannot be accounted for a priori during regularization calibration. The results demonstrate that geometric mesh dependence becomes dominant for large elements and cannot be completely compensated for by regularization.

6. Conclusion

Crash simulation with coarse finite element meshes requires robust regularization strategies. This work presents a numerical calibration procedure for GISSMO that provides stress-state-dependent regularization for shell elements within the framework of plane stress assumptions and von Mises plasticity with isotropic hardening. The resulting calibration exhibits stable and physically consistent trends, most notably a monotonic reduction of the failure strain with increasing element size. The procedure reproduces characteristic features of established stress-state-dependent concepts – such as the absence of regularization in shear and biaxial tension – without prescribing these dependencies a priori.

Beyond reproducing known regularization behavior, the results clarify where regularization can and cannot compensate for coarse meshes. On coupon level, the approach yields reliable scaling and supports key assumptions commonly used in state-of-the-art regularization frameworks. However, regularization is fundamentally bounded by mesh resolution. Once elements become too large, the deformation and the stress states cannot be resolved with sufficient accuracy. No calibration of regularization factors can fully compensate for insufficient mesh resolution. This limitation is particularly critical at the component and full-vehicle level, where the stress state is not prescribed but emerges from the deformation mode. Nominally identical boundary conditions may generate different stress state histories on different meshes. This implies that robust regularization requires not only parameter scaling but also sufficient geometric fidelity to preserve the relevant deformation mechanisms and stress-state evolution.

The present study demonstrates the method for a single material with and without softening. Since the plastic flow response strongly influences the regularization behavior, future work should extend the calibration to additional materials and hardening characteristics to assess transferability. In addition, the roles of the instability curve and softening should be investigated more systematically, as both are expected to affect the accuracy of stress-state-dependent regularization, especially for complex loading paths.

CRediT authorship contribution statement

Thomas Zink: Writing – original draft, Visualization, Validation, Methodology, Investigation, Formal analysis, Conceptualization. **Frank Burbulla:** Writing – review & editing. **Thomas Böhlke:** Writing – review & editing.

Declaration of competing interest

The authors declare that they have no known competing financial interests or personal relationships that could have appeared to influence the work reported in this paper.

Acknowledgment

The research presented in this paper was conducted as part of an industrial PhD project at Dr. Ing. h.c. F. Porsche AG, whose support is greatly appreciated.

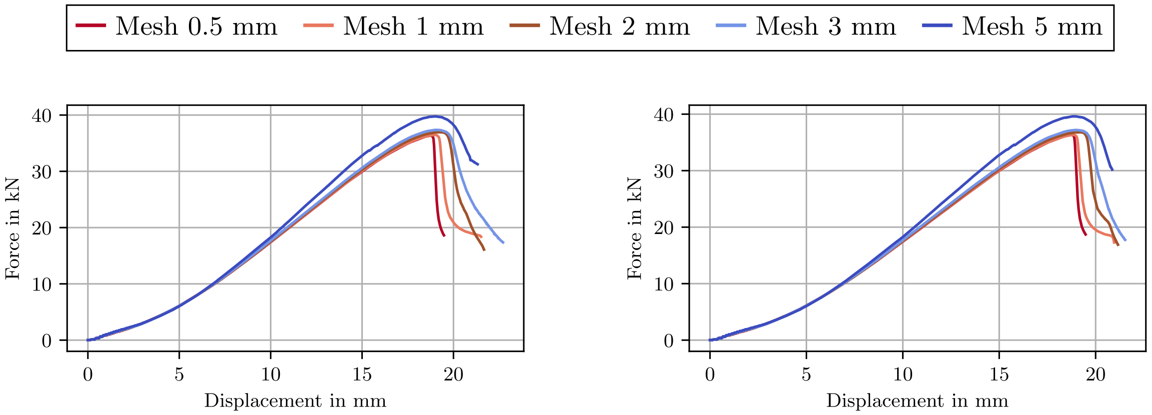

(a) No regularization

(b) Approach A

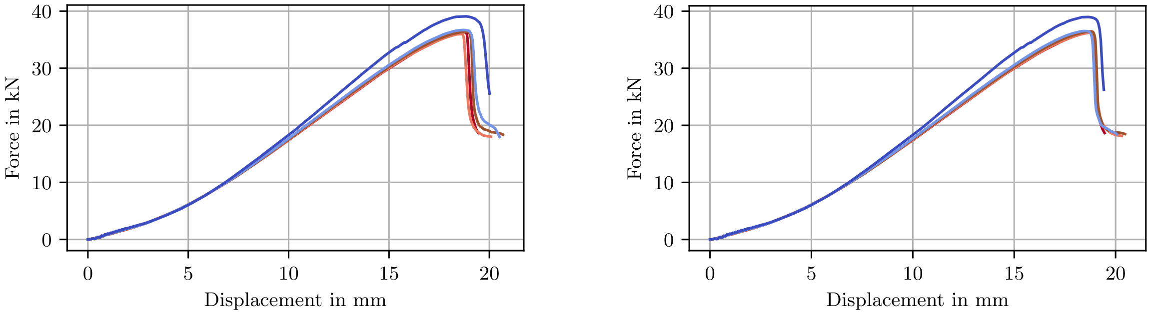

(c) Approach B

(d) Approach C

Fig. 14. Force–displacement curves for the Nakajima 85 specimen without regularization and with regularization Approaches A–C for mesh sizes 0.5, 1, 2, 3 and 5 mm. The curves show little mesh dependence.

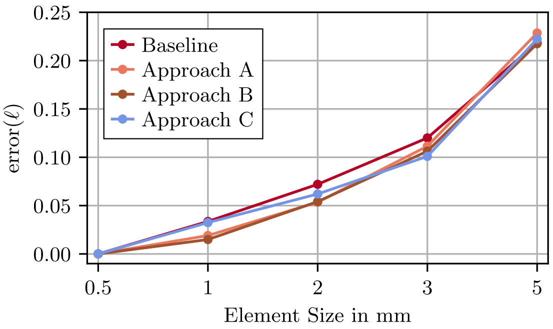

Fig. 15. Mechanical work errors in the crush test for different regularization approaches. For all approaches, the error increases monotonically with element size.

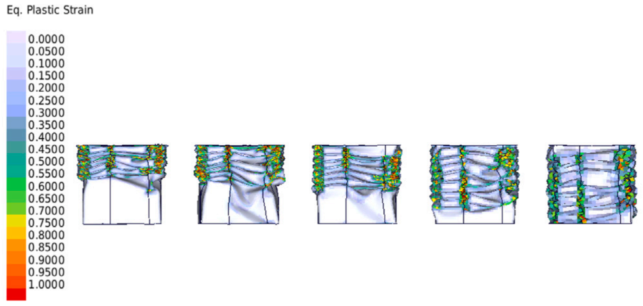

Fig. 16. Distribution of equivalent plastic strain in the crush test without regularization for mesh sizes 0.5, 1, 2, 3 and 5 mm.

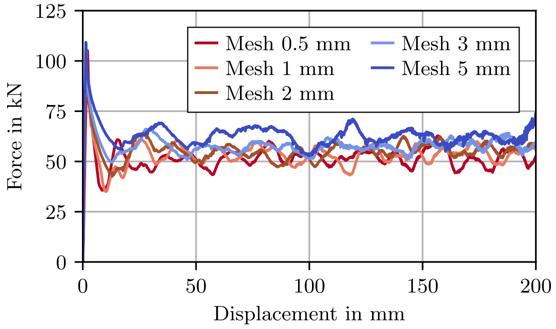

Fig. 17. Force–displacement curve in the crush test without regularization for mesh sizes 0.5, 1, 2, 3 and 5 mm.

Appendix. Results without softening

A.1. Regularization approaches

To further assess the robustness of the proposed regularization approach and to separate the influence of softening from that of reducing the failure strain, an additional material card without softening is considered. In this case, damage does not affect the stress response prior to failure.

The three regularization approaches described in Section 5.3, together with the baseline simulation without regularization, are considered. The results are evaluated both on the element level and for tensile and Nakajima specimens.

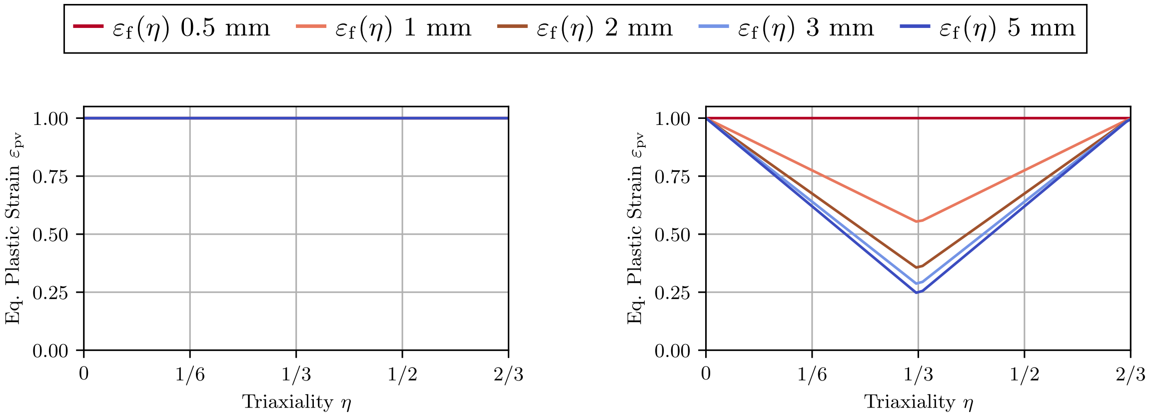

(a) No regularization

(b) Approach A

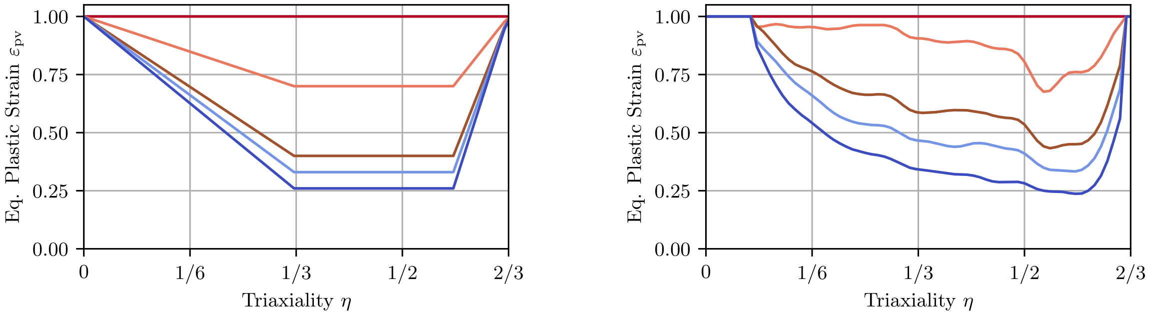

(c) Approach B

(d) Approach C

Fig. A.18. Failure curves for different regularization approaches without softening. The regularization factors differ when softening is not used.

Fig. A.18 shows the resulting regularization curves. Compared to the material card with softening, the minimum failure strain is reduced for all element sizes, especially for large elements. As before, Approach A is limited to a bilinear and Approach B to a trilinear stress-state dependence. Approach C exhibits significant nonlinearity and shows some changes in shape compared to the approach with softening.

A.2. Results on element level

The error in terms of mechanical work (see Fig. A.19) shows behavior comparable to that observed for the material with softening. Without softening, the mechanical work is overestimated for coarse meshes, with maximum errors of up to 60 %. Compared to the material with softening, the average errors increase for coarse meshes because the additional regularization effect induced by softening is absent. For Approach A, the largest errors are observed for stress states close to plane strain at $\eta = 1/\sqrt{3}$. In this regime, the mechanical work is overestimated for all mesh sizes. Approach B again improves this behavior and shows good mesh convergence across the triaxiality space. Since Approaches A and B apply regularization also at low triaxialities, where no localization occurs, the mechanical work is underestimated in this regime. Approach C performs better for stress states close to uniaxial tension and yields the smallest error on average. Again, numerical scatter is observed in the error calculation.

A.3. Results on specimen level

The different regularization approaches are evaluated for a tensile specimen and three Nakajima specimens, cf. Fig. 8. The error calculation follows the procedure described in Section 5.5. The resulting errors are shown in Fig. A.20 and the average errors across all specimens are summarized in Table A.2. Without regularization, errors of up to 300 % are observed. The error increases monotonically with element size. For Approach A, the error is reduced for all specimens. For the tensile test, i.e., the calibration load case, the error is minimal for all element sizes. The Nakajima 15 and Nakajima 85 tests also show reduced errors. However, the Nakajima 45 test still exhibits errors of up to nearly 200 %. Approach B improves the results for the Nakajima 45 test, but underestimates the work for the Nakajima 15 test. Here, abrupt failure after the onset of localization in coarse meshes reduces the mechanical work. The tensile test and the Nakajima 85 test again show very good mesh convergence. The average error is lowest for element sizes up to 3 mm. Approach C shows a larger error for the tensile test, as it has not been specifically calibrated to this load case. For the other specimens, it yields the lowest error among all approaches for the 5 mm mesh.

Table A.2
Mean absolute relative work error (Eq. (27)) for different regularization approaches and shell element edge lengths without softening. The error increases monotonically with element size.

Approach	1 mm	2 mm	3 mm	5 mm
Baseline	0.124	0.447	0.725	1.188
A	0.083	0.257	0.360	0.533
B	0.057	0.087	0.158	0.202
C	0.065	0.099	0.159	0.176

Data availability

Data will be made available on request.

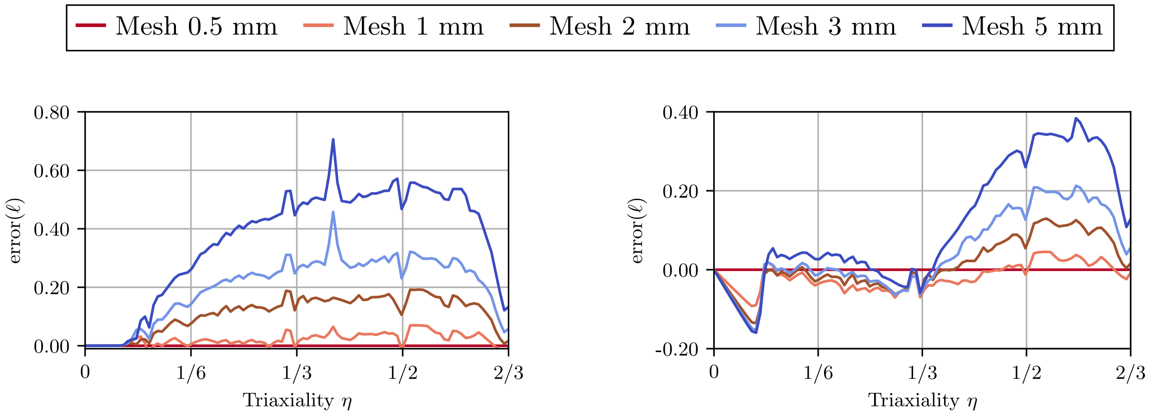

(a) No regularization

(b) Approach A

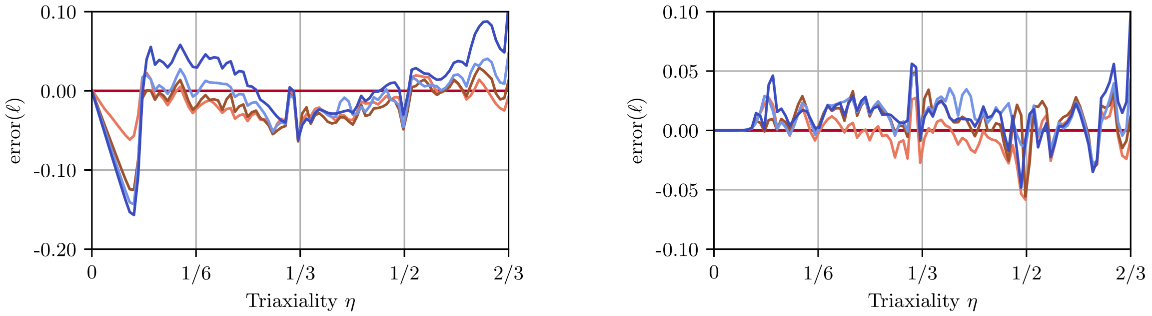

(c) Approach B

(d) Approach C

Fig. A.19. Element-level errors for different regularization approaches as a function of stress triaxiality. The magnitude and variability of the error differ significantly between the approaches and depend on the element size.

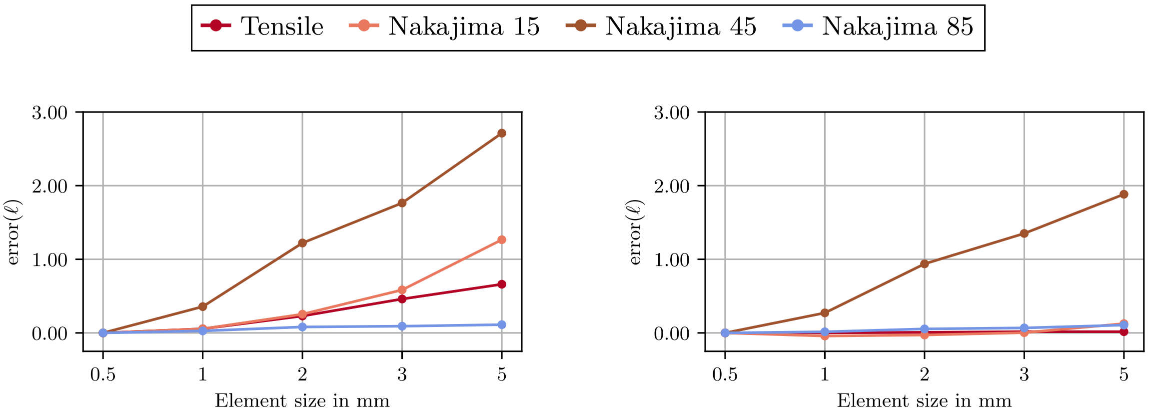

(a) No regularization

(b) Approach A

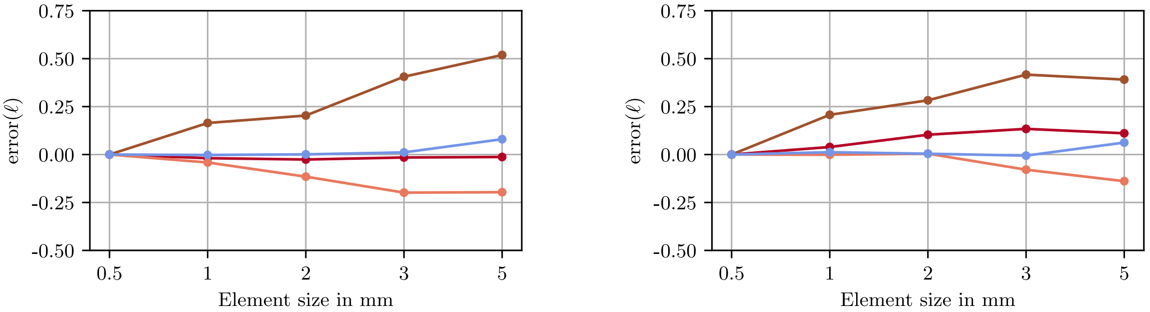

(c) Approach B

(d) Approach C

Fig. A.20. Specimen-level errors for different regularization approaches. The highest error is observed for the Nakajima 45 specimen.

References

Abed-Meraim, F., Balan, T., Altmeyer, G., 2014. Investigation and comparative analysis of plastic instability criteria: Application to forming limit diagrams. Int. J. Adv. Manuf. Technol. 71 (5–8), 1247–1262. http://dx.doi.org/10.1007/s00170-013-5530-8.

Anderson, D., Butcher, C., Pathak, N., Worswick, M., 2017. Failure parameter identification and validation for a dual-phase 780 steel sheet. Int. J. Solids Struct. 124, 89–107. http://dx.doi.org/10.1016/j.ijsolstr.2017.06.018.

Andrade, F., DuBois, P., Feucht, M., Graf, T., Conde, S., Haufe, A., 2022. Instability and mesh dependence - part II. In: 16th LS-DYNA Forum. Bamberg, Germany.

Andrade, F., Erhart, T., Feucht, M., 2023. Stress state dependent regularization. In: North American LS-DYNA Forum. Bamberg, Germany.

Andrade, F.X.C., Feucht, M., Haufe, A., Neukamm, F., 2016. An incremental stress state dependent damage model for ductile failure prediction. Int. J. Fract. 200 (1–2), 127–150. http://dx.doi.org/10.1007/s10704-016-0081-2.

Andrade, F.X., Pires, F.M.A., De Sá, J.M.C., Malcher, L., 2009. Nonlocal integral formulation for a plasticity-induced damage model. Comput. Methods Mater. Sci. 9, 49–54. http://dx.doi.org/10.7494/cmms.2009.1.0207.

ANSYS Inc., 2023. LS-DYNA Theory Manual.

Bažant, Z.P., Jirásek, M., 2002. Nonlocal integral formulations of plasticity and damage: Survey of progress. J. Eng. Mech. 128 (11), 1119–1149. http://dx.doi.org/10.1061/(ASCE)0733-9399(2002)128:11(1119).

Belytschko, T., Lasry, D., 1989. A study of localization limiters for strain-softening in statics and dynamics. Comput. Struct. 33 (3), 707–715. http://dx.doi.org/10.1016/0045-7949(89)90244-7.

Besson, J., 2010. Continuum models of ductile fracture: A review. Int. J. Damage Mech. 19 (1), 3–52. http://dx.doi.org/10.1177/1056789509103482.

Bouktir, Y., Chalal, H., Abed-Meraim, F., 2018. Prediction of necking in thin sheet metals using an elastic–plastic model coupled with ductile damage and bifurcation criteria. Int. J. Damage Mech. 27 (6), 801–839. http://dx.doi.org/10.1177/1056789517704030.

Chaboche, J.L., 1988. Continuum damage mechanics: Part I—general concepts. J. Appl. Mech. 55 (1), 59–64. http://dx.doi.org/10.1115/1.3173661.

Chen, X., Chen, G., Huang, L., 2018. Validation of GISSMO model for fracture prediction of a third-generation advanced high-strength steel. SAE Int. J. Mater. Manuf. 11 (4), 293–302. http://dx.doi.org/10.4271/2018-01-0107.

Chen, L., Zhu, B., Wu, Z., Hu, B., Li, Y., Guo, Y., 2024. Deformation and failure behavior of 2024-T42 sheet under impact loading. Thin-Walled Struct. 203, http://dx.doi.org/10.1016/j.tws.2024.112230.

Choi, S., Shin, J., Suh, J., Kim, D., 2024. Modeling asymmetric fracture mechanics of Mg alloy wire in drawing process. J. Magnes. Alloy. 12 (5), 2057–2069. http://dx.doi.org/10.1016/j.jma.2024.05.020.

Cockcroft, M., Latham, D., 1968. Ductility and the workability of metals. J. Inst. Met. 96.

Costas, M., Morin, D., Hopperstad, O.S., Børvik, T., Langseth, M., 2019. A through-thickness damage regularisation scheme for shell elements subjected to severe bending and membrane deformations. J. Mech. Phys. Solids 123, 190–206. http://dx.doi.org/10.1016/j.jmps.2018.08.002.

Dai, M., Ying, L., Wang, S., Ma, H., Hu, P., Wang, Y., 2022. Modeling the crashworthiness analysis of functional graded strength thin-walled structure with phenomenological GISSMO model. Thin-Walled Struct. 180, http://dx.doi.org/10.1016/j.tws.2022.109766.

Davaze, V., Feld-Payet, S., Vallino, N., Langrand, B., Besson, J., 2023. A non-local approach for Reissner–Mindlin shell elements in dynamic simulations: Application with a Gurson model. Comput. Methods Appl. Mech. Engrg. 415, 116142. http://dx.doi.org/10.1016/j.cma.2023.116142.

De Souza Neto, E.A., Perić, D., Owen, D.R.J., 2008. Computational Methods for Plasticity: Theory and Applications, first ed. Wiley, http://dx.doi.org/10.1002/9780470694626.

DuBois, P., Andrade, F., Feucht, M., Graf, T., Conde, S., Haufe, A., 2022. Instability and mesh dependence - Part I. In: 16th LS-DYNA Forum. Bamberg, Germany.

Effelsberg, J., Haufe, A., Feucht, M., Neukamm, F., Du Bois, P., 2012. On parameter identification for the GISSMO damage model. In: 12th International LS-DYNA Users Conference. Detroit, Michigan, USA.

Forest, S., Lorentz, E., 2004. Localization phenomena and regularization methods. In: Local Approach To Fracture. Vol. 1, Presses des Mines Paris, pp. 311–371.

Geers, M.G.D., Brekelmans, W.A.M., Borst, R., 1994. Viscous regularization of strain-localisation for damaging materials. In: Kusters, G.M.A., Hendriks, M.A.N. (Eds.), DIANA Computational Mechanics 84. Springer Netherlands, Dordrecht, pp. 127–138.

Gu, B., Lim, J., Hong, S., 2022. Determination and verification of GISSMO fracture properties of bolts used in radioactive waste transport containers. Materials 15 (5), http://dx.doi.org/10.3390/ma15051893.

Guo, J., Liu, H., Li, X., Yang, T., 2023. Fracture behavior of the hot-stamped PHS2000 steel based on GISSMO failure model. Metals 13 (8), http://dx.doi.org/10.3390/met13081360.

Guo, J., Wang, L., Jiang, T., Wang, F., Liu, H., Li, X., Chang, Y., 2024. Fracture behaviors of the 1500 MPa-grade anti-oxidation hot-stamped steel: Measurement, numerical simulation and experimental validation. Mater. Today Commun. 40, http://dx.doi.org/10.1016/j.mtcomm.2024.109523.

Gurson, A.L., 1977. Continuum theory of ductile rupture by void nucleation and growth: Part I—yield criteria and flow rules for porous ductile media. J. Eng. Mater. Technol. 99 (1), 2–15. http://dx.doi.org/10.1115/1.3443401.

Hill, R., 1958. A general theory of uniqueness and stability in elastic-plastic solids. J. Mech. Phys. Solids 6 (3), 236–249. http://dx.doi.org/10.1016/0022-5096(58)90029-2.

Hong, S., Kim, J., Jun, T., 2019. Failure prediction for the tearing of a pin-loaded dual phase steel (DP980) adjusting guide. Appl. Sci. 9 (24), http://dx.doi.org/10.3390/app9245460.

Johnson, G.R., Cook, W.H., 1985. Fracture characteristics of three metals subjected to various strains, strain rates, temperatures and pressures. Eng. Fract. Mech. 21 (1), 31–48. http://dx.doi.org/10.1016/0013-7944(85)90052-9.

Jurendic, S., Anderson, D., 2019. Characterizing damage and fracture of sheet metal materials using large scale test specimen. IOP Conf. Ser.: Mater. Sci. Eng. 651 (1), 012059. http://dx.doi.org/10.1088/1757-899X/651/1/012059.

Kõrgesaar, M., Remes, H., Romanoff, J., 2014. Size dependent response of large shell elements under in-plane tensile loading. Int. J. Solids Struct. 51 (21–22), 3752–3761. http://dx.doi.org/10.1016/j.ijsolstr.2014.07.012.

Lauff, C., Schneider, M., Böhlke, T., 2026. Numerically robust local continuum damage models with softening response via convex relaxation. Comput. Methods Appl. Mech. Engrg. 452, 118759. http://dx.doi.org/10.1016/j.cma.2026.118759.

Lee, S.-K., Lee, J.-S., Song, J.-H., Park, J.-Y., Choi, S., Noh, W., Kim, G., 2018. Fracture simulation of cold roll forming process for aluminum 7075-T6 automotive bumper beam using GISSMO damage model. In: Abe, Y., Mori, K.-I., Maeno, T. (Eds.), Procedia Manufacturing. Vol. 15, Elsevier B.V., pp. 751–758. http://dx.doi.org/10.1016/j.promfg.2018.07.314.

Lemaitre, J., 1985. A continuous damage mechanics model for ductile fracture. J. Eng. Mater. Technol. 107 (1), 83–89. http://dx.doi.org/10.1115/1.3225775.

Mehari, Z., Han, J., 2022. Numerical prediction of ductile fracture during the partial heating roll forming process of DP980. Int. J. Fract. 234 (1–2), 97–112. http://dx.doi.org/10.1007/s10704-021-00572-5.

Mohamed, M., Amer, M., Shazly, M., Masters, I., 2021. Assessment of different ductile damage models of AA5754 for cold forming. Int. J. Adv. Manuf. Technol. 114 (3–4), 1219–1231. http://dx.doi.org/10.1007/s00170-021-06836-7.

Mou, H., Chen, Y., Xie, J., Liu, H., 2025. Crashworthiness analysis of single CFRP, hybrid CFRP/Al and fiber metal laminate C-channels: Quasi-static crushing tests and numerical simulations. Thin-Walled Struct. 213, http://dx.doi.org/10.1016/j.tws.2025.113226.

Needleman, A., 1988. Material rate dependence and mesh sensitivity in localization problems. Comput. Methods Appl. Mech. Engrg. 67 (1), 69–85. http://dx.doi.org/10.1016/0045-7825(88)90069-2.

Neukamm, F., 2018. Lokalisierung und Versagen von Blechstrukturen (Ph.D. thesis). Universität Stuttgart, http://dx.doi.org/10.18419/OPUS-10082.

Niazi, M.S., Wisselink, H.H., Meinders, T., 2013. Viscoplastic regularization of local damage models: Revisited. Comput. Mech. 51 (2), 203–216. http://dx.doi.org/10.1007/s00466-012-0717-7.

Pack, K., Mohr, D., 2017. Combined necking & fracture model to predict ductile failure with shell finite elements. Eng. Fract. Mech. 182, 32–51. http://dx.doi.org/10.1016/j.engfracmech.2017.06.025.

Pack, K., Tancogne-Dejean, T., Gorji, M.B., Mohr, D., 2018. Hosford-Coulomb ductile failure model for shell elements: Experimental identification and validation for DP980 steel and aluminum 6016-T4. Int. J. Solids Struct. 151, 214–232. http://dx.doi.org/10.1016/j.ijsolstr.2018.08.006.

Rabczuk, T., 2013. Computational methods for fracture in brittle and quasi-brittle solids: State-of-the-art review and future perspectives. ISRN Appl. Math. 2013, 1–38. http://dx.doi.org/10.1155/2013/849231.

Samadian, P., Ten Kortenaar, L., Omer, K., Butcher, C., Worswick, M., 2020. Fracture characterization of tailored Usibor® 1500-AS and damage modelling based on a coupled-micromechanical-phenomenological strategy. Eng. Fract. Mech. 223, http://dx.doi.org/10.1016/j.engfracmech.2019.106785.

Schauwecker, F., Moncayo, D., Middendorf, P., 2022. Characterization of high-strength bolts and the numerical representation method for an efficient crash analysis. Eng. Fail. Anal. 137, 106249. http://dx.doi.org/10.1016/j.engfailanal.2022.106249.

Schwarz, S., Junker, P., Hackl, K., 2021. Variational regularization of damage models based on the emulated RVE. Contin. Mech. Thermodyn. 33 (1), 69–95. http://dx.doi.org/10.1007/s00161-020-00886-0.

Storheim, M., Alsos, H.S., Hopperstad, O.S., Amdahl, J., 2015. A damage-based failure model for coarsely meshed shell structures. Int. J. Impact Eng. 83, 59–75. http://dx.doi.org/10.1016/j.ijimpeng.2015.04.009.

Swift, H., 1952. Plastic instability under plane stress. J. Mech. Phys. Solids 1 (1), 1–18. http://dx.doi.org/10.1016/0022-5096(52)90002-1.

Tvergaard, V., Needleman, A., 1984. Analysis of the cup-cone fracture in a round tensile bar. Acta Metall. 32 (1), 157–169. http://dx.doi.org/10.1016/0001-6160(84)90213-X.

Walters, C.L., 2014. Framework for adjusting for both stress triaxiality and mesh size effect for failure of metals in shell structures. Int. J. Crashworthiness 19 (1), 1–12. http://dx.doi.org/10.1080/13588265.2013.825366.

Wei, L., Qin, F., Cui, K., 2021. Prediction the stainless steel sheet fracture with mesh size effect for shell elements. Int. J. Solids Struct. 210–211, 35–48. http://dx.doi.org/10.1016/j.ijsolstr.2020.11.013.

Werling, T., Baumann, G., Feist, F., Sinz, W., Ellersdorfer, C., 2021. On the dynamic electro-mechanical failure behavior of automotive high-voltage busbars using a split hopkinson pressure bar. Materials 14 (21), http://dx.doi.org/10.3390/ma14216320.

Werling, T., Sprenger, M., Ellersdorfer, C., Sinz, W., 2020. Experimental and numerical investigation of the behavior of automotive battery busbars under varying mechanical loads. Energies 13 (24), http://dx.doi.org/10.3390/en13246572.

Wiegard, B., Ehlers, S., 2020. Pragmatic regularization of element-dependent effects in finite element simulations of ductile tensile failure initiation using fine meshes. Mar. Struct. 74, 102823. http://dx.doi.org/10.1016/j.marstruc.2020.102823.

Xiao, Y., Hu, Y., 2019. An extended iterative identification method for the GISSMO model. Metals 9 (5), 568. http://dx.doi.org/10.3390/met9050568.

Yamada, Y., Pedersen, P.T., Endo, H., 2005. Numerical study on the effect of buffer bow structure in ship-ship collision. In: ISOPE International Ocean and Polar Engineering Conference. ISOPE, pp. ISOPE–I.

Yao, R., Zhang, B., Niu, Q., Li, Q., Sun, G., 2025. On modeling of extruded thin-walled multi-cell structures incorporating anisotropy yielding, strain hardening and damage failure. Thin-Walled Struct. 216, http://dx.doi.org/10.1016/j.tws.2025.113548.

Zink, T., Burbulla, F., Böhlke, T., 2025. Energy-based regularization approaches for GISSMO. In: 2025 Ansys EMEA Transportation Summit and LS-DYNA Conference. Munich, Germany.